2003-12-01

Modelling Growth and Testing of Multilayer Cavity Structures Incorporating Birefringent Materials

Nour-eddine El Khachia
Technological University Dublin

MODELLING GROWTH AND TESTING OF MULTILAYER CAVITY STRUCTURES INCORPORATING BIREFRINGENT MATERIALS.

by

Nour-eddine El khachia B.Sc (Appl. Sc)

A thesis submitted for the degree of Master of Philosophy to the Department of Physics Dublin Institute of Technology

Supervisors: Dr. Paul Horan
Dr. John Doran.

School of Physics
Dublin Institute of Technology
December 2003

This thesis is dedicated to my mother, Aicha Al mohamadi.

Table of contents

Abstract

A simple one-dimensional photonic bandgap structure, which is also known as a Fabry-Perot Microcavity (FPM) structure was studied theoretically and experimentally. In particular this project addressed introducing an optically birefringent material in the cavity. This FPM consists of two grown regular Distributed Bragg Reflector (DBR) mirrors that can be put together as a sandwich with a space between them, which will lead to the creation of the desired cavity. Each mirror, or one-dimensional dielectric stack structure, was grown using the Vacuum Evaporation Technique and consists of multiple layers of alternating high-and low-refractive index dielectric materials arranged periodically.

The project covers making multilayer structures, phase shift analysis, modelling and measuring structures incorporating birefringent materials in the cavity.

Results show an agreement between modelling and experimental measurements of transmission spectra of multilayer cavity structures incorporating birefringent materials.

Acknowledgements

If I have succeeded in these tasks, it is only because of the assistance of my supervisors and colleagues.

I would like to thank a lot Dr. Paul Horan and Dr. John Doran, my research supervisors, for their guidance and help throughout my research.

In particular, I would like to thank Dr. Hugh Byrne for his help, continuous encouragement and for taking care of any administration problems within DIT, which was not easy at the start.

In addition I gratefully thank David Fleming, FOCAS technician, for his help at the start of this project, with the LABVIEW program, making thin-films and ordering materials.

I would like also to thank Shane Linnane, another FOCAS technician for his contribution in making thin-films. Thanks also to all the staff of the Physics department in Kevin Street for any valuable assistance.

Finally I would like to thank all my colleagues for making my time in DIT Kevin Street so enjoyable.

Nour-eddine El Khachia

1. Introduction and theory.

Photonic bandgap (PBG) and microcavities structures are structures on the scale of a wavelength and they are playing an increasingly important role in the development of highly effective light emitters [1-3]. They are resonators that can be 1, 2 or 3-dimensional and they enable us to control the optical emission properties of materials placed inside them.

These artificial one, two-and three-dimensionally periodic structures can be called photonic crystals [4-6]. They can be fabricated in an optical material (crystal or amorphous) with unit cells whose dimensions are comparable to the optical wavelength.

Essentially photonic crystals consist of regularly arranged dielectric scatterers at the wavelength scale (i.e. ~0.5 nm), exhibiting band gaps to photons, analogous for the case of electrons in semiconductors.

Since the first proposals of a photonic bandgap (PBG) effect by Yablonovitch, this subject has received rapidly increasing research interest [7]. Many new ideas and applications are being pursued in metallic, dielectric, and acoustic structures. There have been many published theoretical works aimed at understanding the changes and effects inside a photonic bandgap on spontaneous emission, optical modes and zero-point fluctuations [8-11].

But from the point of view of this project we intended to look at a one-dimensional photonic bandgap structure, which is known as the Fabry-Perot cavity structure (Appendix F).

A simple cavity structure consists of two regular Distributed Bragg Reflectors (DBR) that can be put together, as a sandwich, with a thin spacing, which will lead to the creation of a desired cavity [12]. This latter combination of two DBR mirrors with a cavity between them is known as the Fabry-Perot resonator [13-16].

Each mirror, or one-dimensional dielectric stack structure, consists of multiple layers of alternating high-and low-index dielectric materials arranged periodically [17].

The thickness of each layer is chosen so as to satisfy the Bragg quarter-wave condition, that is:

$$d = \frac{\lambda_0}{4n} \tag{1.1}$$

where λ_0 is the reference wavelength of the structure, and d and n are the thickness and the real part of the linear refractive index of a particular layer, respectively.

The aim of this project is to investigate the polarisation effects on light in multilayer cavity structures incorporating birefringent materials, an area that has only recently become of interest in exploring multilayer structures. The most recent study of one-dimensional optical microcavities based on dielectric mirrors with a birefringent material has been investigated by Virgili and Bradley, who they managed to get a completely polarised photoluminescence emission from a microcavity containing an aligned conjugated polymer [18]. In that publication the photoluminescence emission light from a microcavity structure, for different polarisation states, was studied when the birefringence of an in-plane aligned liquid crystal conjugated polymer (poly (9,9-dioctylfluorene)) was combined with the normal to plane mode selective properties of a vertical optical microcavity [19].

The microcavity structure consisted of two mirrors, typically separated by a few hundred nanometers. The first mirror of the cavity was a high reflectivity DBR, consisting of alternating quarter-wave layers of silicon dioxide (n=1.45) and silicon nitride (n=1.95). On top of the DBR, Virgili et al deposited a very thin layer of polyimide, which was rubbed mechanically using a felt cloth in order to create a surface that can be used to align liquid crystal materials. A layer of the poly (9,9-dioctyl-fluorene) was then spin-coated onto the alignment layer, followed by thermal evaporation of an aluminium mirror to complete the cavity.

The study of this one-dimensional microcavity structure, and the way the cavity was constructed in that publication is similar to our approach when investigating and designing the cavity to be studied in this project.

Our cavity structure consists of two mirrors, separated by a quarter wave-plate of a birefringent material such as polyvinyl-alcohol (PVA). The DBR mirrors consisting of alternating quarter-wave layers of Zinc Sulfide (n=2.36) and Magnesium Fluoride (n=1.38) are grown using a vacuum evaporation technique (Appendix G). By placing a birefringent material within the cavity, it is then possible to measure the transmitted light going through the structure with different polarisation states. These results were then compared to model calculations written in the Matlab environment (The Math works). A schematic of the DBRs used is shown below in figure 1.1

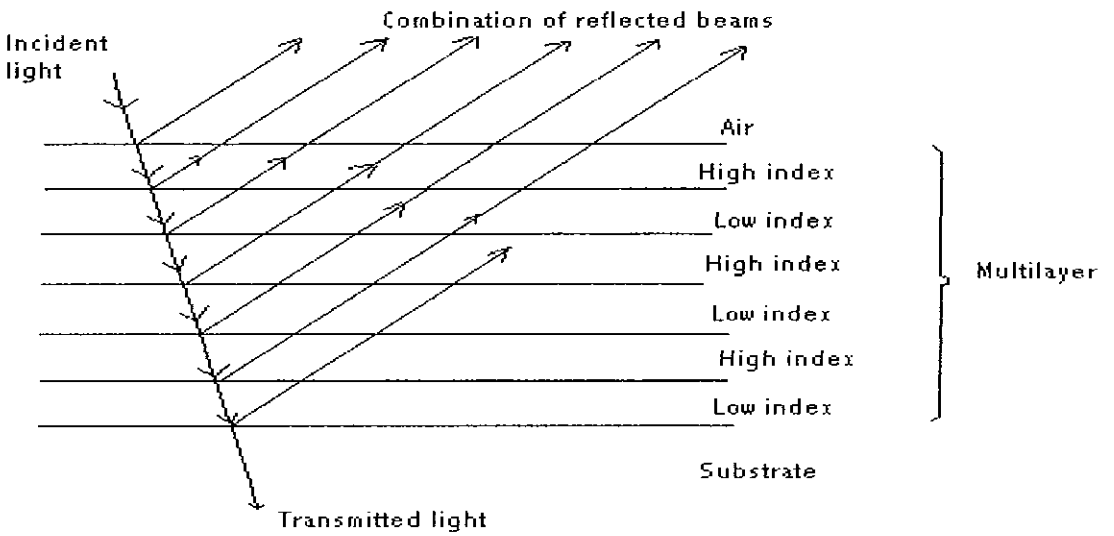

Fig. 1.1. A multilayer Structure of high and low refractive indices showing the transmitted and the reflected light of one single beam.

In figure 1.1, it can be seen that the various components of the incident light produced by reflection successive boundaries throughout the assembly will reappear at the front surface all in phase, if the layer thickness is chosen to be quarter wave thick so that they will interfere constructively [21]. This means that the effective reflectance of the assembly can be made as high as required by increasing the number of layers. In general the areas of study to be carried out in this project can be summarised as follow:

- Commission new evaporator unit.
- Model the test structures using MATLAB software with or without dispersion.
- Making multilayer thin films structures of ZnS and MgF_2 using the vacuum evaporation technique.
- Run the UV-vis spectrum of each film in order to characterise it spectroscopically.
- Phase shift analysis of any multilayer cavity structure.

1.1. Thin film theory for modelling multi-layered structures.

The initial aim is to find mathematically R (reflectance) and T (transmittance) for a linearly polarised wave (shown in Fig. 1.1) incident on a thin dielectric film (that is deposited on a substrate) with a thickness of only a fraction of a wavelength [20]. It is firstly necessary to carry out the mathematics for a single layer structure and then move on to a multi-layered structure.

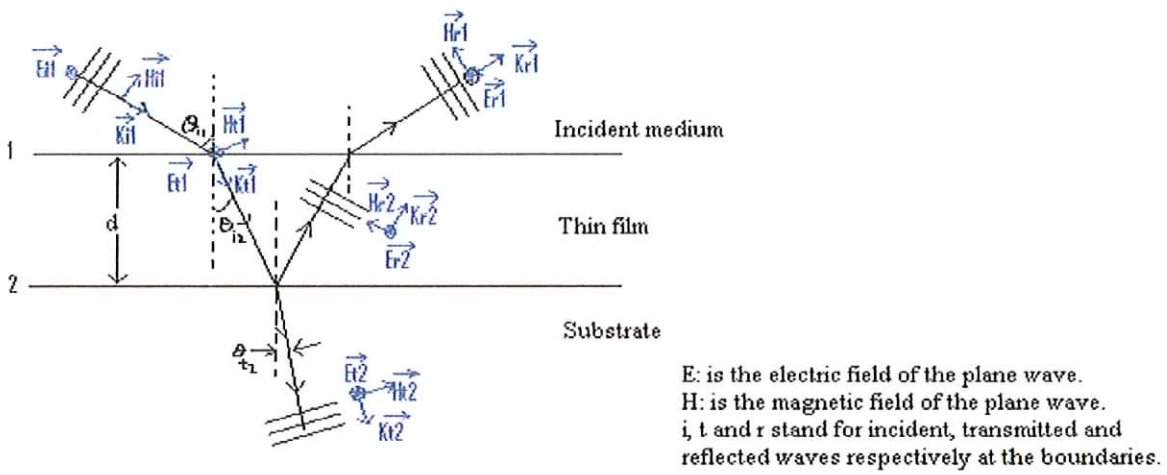

Fig.1.2. Schematic diagram of the E and H fields at the boundaries of a single layer

The standard type of calculation in this section is based on solutions of Maxwell's Equations. So before starting these calculations [21], it is necessary to take some considerations into account:

- Each component of the electric or magnetic fields represents the resultant of all possible waves travelling in that direction at that point in the medium.

- The tangential components of both the E and H fields have to be continuous across the boundaries.
- The refractive indices of each medium are considered real; therefore absorption term will not be taken into account at this stage of calculations.

So, at boundary 1:

$$E_1 = E_{i1} + E_{r1} = E_{t1} + E'_{r2} \tag{1.2}$$

and

$$H_1 = \sqrt{\frac{\varepsilon_o}{\mu_o}} (E_{i1} - E_{r1}) n_0 \cos(\theta_{i1})$$

$$= \sqrt{\frac{\varepsilon_o}{\mu_o}} (E_{i1} - E'_{r2}) n_1 \cos(\theta_{i2}) \tag{1.3}$$

Where n_0, n_1, n_s, are the refractive indices of air, film and the substrate, and i, r and t refer to incident, reflected and transmitted waves respectively.

At boundary 2: $$E_2 = E_{i2} + E_{r2} = E_{t2} \tag{1.4}$$

and

$$H_2 = \sqrt{\frac{\varepsilon_o}{\mu_o}} (E_{i2} - E_{i2}) n_1 \cos(\theta_{i2})$$

$$= \sqrt{\frac{\varepsilon_o}{\mu_o}} E_{t2} \cos(\theta_{t2}) \tag{1.5}$$

When the wave traverses the film, it undergoes a phase shift of $k_0 \times h$, where k_0 is the wave number, $k_0 = 2\pi / \lambda$, and $h = 2\, n_1 d \cos(\theta_{i2})$.

Thus the incident and reflected electric waves at the boundary 2 can be expressed as follows:

$$E_{i2} = E_{t1} \exp(-ik_0 h)$$

and

$$E_{i2} = E_{r2} \exp(ik_0 h)$$

Hence equations (1.4) and (1.5) can be written as:

$$\mathbf{E}_2 = E_{i\,1} \exp(-ik_0h) + E'_{r\,2} \exp(ik_0h) \tag{1.6}$$

and $$H_2 = (E_{i\,1} \exp(-ik_0h) - E_{r\,2} \exp(ik_0h)) \sqrt{\frac{\varepsilon_o}{\mu_o}}\ n_1 \cos(\theta_{1\,2}) \tag{1.7}$$

Equations (1.6) and (1.7) can be solved for $E_{i\,1}$ and $E'_{r\,2}$, which when substituted into equations (1.2) and (1.3), will give:

$$E_1 = E_2 \cos(k_0h) + H_2 (i \sin(k_0h)) / Y_1 \tag{1.8}$$

and $$H_1 = E_2\, Y_1\, i \sin(k_0h) + H_2 \cos(k_0h) \tag{1.9}$$

where $$Y_1 = \sqrt{\frac{\varepsilon_o}{\mu_o}}\ n_1 \cos(k_0h)$$

Hence equations (1.8) and (1.9), can be represented in matrix notation as follows:

$$\begin{bmatrix} E_1 \\ H_1 \end{bmatrix} = \begin{bmatrix} \cos k_0h & (i \sin k_0h)/Y_1 \\ Y_1 i \sin k_0h & \cos k_0h \end{bmatrix} \begin{bmatrix} E_2 \\ H_2 \end{bmatrix}$$

$$\Rightarrow \quad \begin{bmatrix} E_1 \\ H_1 \end{bmatrix} = M_1 \begin{bmatrix} E_2 \\ H_2 \end{bmatrix} \tag{1.10}$$

Where M_1 is a characteristic matrix and relates the fields at the two adjacent boundaries.

If two overlaying films are deposited on the substrate, there will be three boundaries and the same procedure will be carried out. Therefore one can write:

$$\begin{bmatrix} E_2 \\ H_2 \end{bmatrix} = M_2 \begin{bmatrix} E_3 \\ H_3 \end{bmatrix} \tag{1.11}$$

Multiplying both sides of equation (1.11) by M_1, we obtain:

$$\begin{bmatrix} E_1 \\ H_1 \end{bmatrix} = M_1 M_2 \begin{bmatrix} E_3 \\ H_3 \end{bmatrix}$$

Hence when we have n layers (each one represented by a characteristic matrix M), the first and the last boundaries are related by:

$$\begin{bmatrix} E_1 \\ H_1 \end{bmatrix} = M_1.M_2.M_3 \ldots \ldots M_n \begin{bmatrix} E_{(n+1)} \\ H_{(n+1)} \end{bmatrix} \tag{1.12}$$

Where the term $(M_1.M_2.M_3 \ldots M_n)$ represents the characteristic matrix of the entire system, which is the resultant of the product of the individual 2×2 matrices.

So we can write: $M = M_1.M_2 \ldots \ldots M_n = \begin{bmatrix} m_{11} & m_{12} \\ m_{21} & m_{22} \end{bmatrix}$

In order to implement these calculations, we firstly need to derive expressions for the amplitude coefficients of reflection and transmission.

$$r = \frac{E_{r1}}{E_{i1}} \qquad \text{coefficient of reflection.} \tag{1.13}$$

$$t = \frac{E_{t2}}{E_{i1}} \qquad \text{the coefficient of transmission.} \tag{1.14}$$

If we try to write equation (1.10) in terms of equations (1.2), (1.3) and (1.4) and set

$$Y_0 = \sqrt{\frac{\varepsilon_o}{\mu_o}}\, n_0 \cos(\theta_{i\,1})$$

and $$Y_s = \sqrt{\frac{\varepsilon_o}{\mu_o}}\, n_s \cos(\theta_{t\,2})$$

We obtain the following equation:

$$\begin{bmatrix} (E_{i1} + E_{r1}) \\ (E_{i1} - E_{r1})Y_0 \end{bmatrix} = M_1 \begin{bmatrix} E_{t2} \\ E_{t2} \times Y_s \end{bmatrix}$$

Which becomes on expansion of the matrices and using equations (1.13) and (1.14):

$$\begin{cases} 1 + r = m_{11}t + m_{12}Y_s t \\ (1 - r)Y_0 = m_{21}t + m_{22}Y_s t \end{cases}$$

By solving the above system of equations for r and t we finally obtain:

$$r = \frac{Y_0 m_{11} + Y_0 Y_s m_{12} - m_{21} - Y_s m_{22}}{Y_0 m_{11} + Y_0 Y_s m_{12} + m_{21} + Y_s m_{22}} \tag{1.15}$$

and $$t = \frac{2Y_0}{Y_0 m_{11} + Y_0 Y_s m_{12} + m_{21} + Y_s m_{22}} \tag{1.16}$$

Therefore to find r or t for any configuration of films, we need only compute the characteristic matrices of each film, multiply them, and then substitute the resulting matrix elements into equation (1.15) and (1.16).

The reflectance (R) and transmittance (T), which are the experimentally measured quantities, are defined as follows:

$$R = r\, r^*$$

$$T = t\, t^*$$

where r* and t* are the conjugate of r and t respectively.

From the point of view of this project a multilayer structure becomes more useful with the introduction of a defect, which is a gap or alternately viewed as a cavity. The cavity can be viewed as a layer that is either too thick or too thin.

1.2. Single layer

The initial experimental work in this project was focused mainly on Zinc Sulfide as a material to be evaporated. Single thin film layers of Zinc Sulfide were deposited on a glass substrate using a vacuum deposition system. These single thin film structures were then modelled and characterised spectroscopically.

In general the main sections covered in this preliminarily investigation were:

(i) Making thin films of ZnS with different thicknesses using the vacuum evaporation technique.

(ii) Characterise each deposited thin-film:

- Its thickness using a Dektak, which is a Stylus measurement instrument.
- The uniformity of the deposited layer on the substrate.

(iii) Measuring the thickness of the deposited layer using a phase-contrast microscope, and compare it with that obtained using the Dektak.

(iv) Running the transmittance spectra of each deposited film using two instruments: the Perkin Elmer UV-vis spectrometer and the CM110 versatile UV-vis spectrometer controlled by a LABVIEW programme for comparison purposes.

(v) Write software to model the optical properties of the multilayer structures. This was done within the MATLAB environment.

1.3. Modelling test structures using MATLAB software.

To carry out these calculations satisfactorily, the Matlab environment was chosen. It allows us to solve many technical computing problems, especially those with matrix and vector formulations such as the problem of interest here [22].

1.3.1. Program structure

To calculate the total reflectance and transmittance of a multi-layered structure using the theory outlined above, computer programs were written. The layout of these programs is summarised in the following diagram:

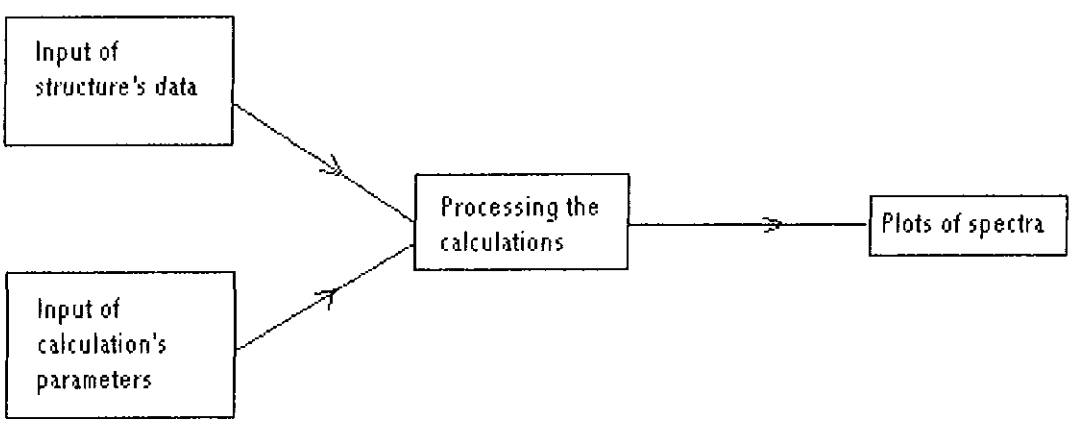

Fig.1.3. Diagram of a typical format of a MATLAB program.

As an example for application, two programs 1 and 2 (Appendix A) were written in order to model the reflectance of two different multi-layered structures against wavelength. The format of these two programs is shown below in figure 1.4.

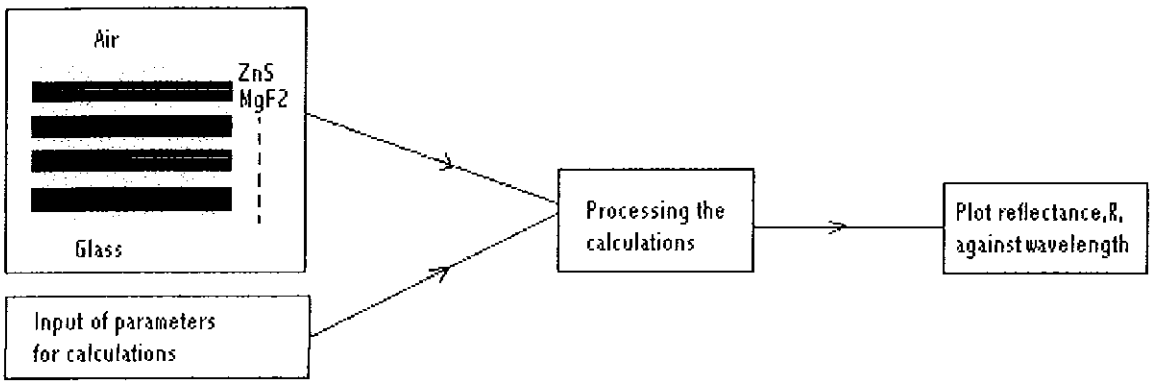

Fig.1.4. Format of programs 1 and 2 (Appendix A).

The first program was written for a nine-layered thin film air/ ZnS, MgF_2 .../glass, and the second one was for a fifteen-layered, air/HLHLHLHLH/glass, structure where L stands for Low-Index Film (MgF_2) and H for High-Index Film (ZnS).

The results obtained from running these programs are represented graphically, as shown in figures 1.5a and 1.5b.

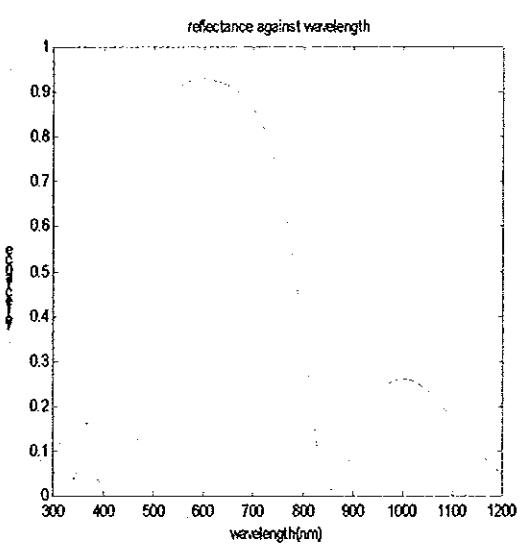

Fig.1.5a. Modelled reflectance for normal incidence of a nine-layer quarter-wavelength stack on glass.

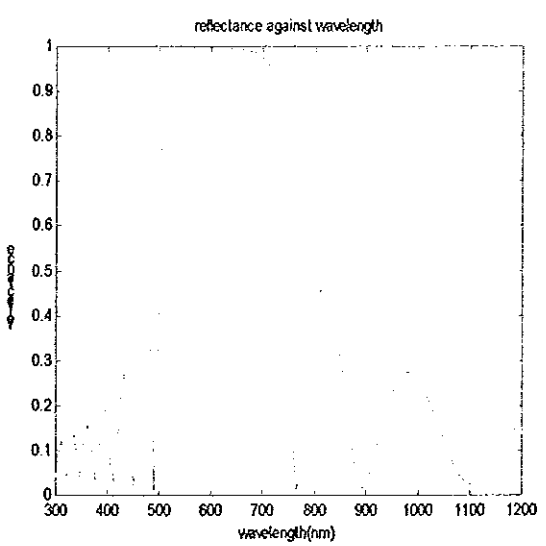

Fig.1.5b. Modelled reflectance for normal incidence of a fifteen-layer quarter-wavelength stack.

Figures 1.5a and 1.5b show the variation of total reflectance against wavelength of a very basic type of thin-film structure. It is a stack of alternate high- and low-index films all one-quarter-wavelength thick. Such structures are used in many areas [23]:

- As long-wave-pass filter, or a short-wave-pass filter.
- As a reflector in a thin-film Fabry-Perot interferometer.

On increasing the number of alternate layers of MgF_2 and ZnS in programme 1, in order to contrast the variations of the reflectivity of the structure, programme 2 was created. The results are represented graphically (as shown in Figure 1.5b).

From figures 1.5a and 1.5b, it is found that the total reflectance remains high ($R > 95\%$) over only a limited range of wavelengths. Outside this zone, the reflectance changes abruptly to a low value, and the number of oscillations is higher at lower wavelength (left of the stop band region) than the ones at higher wavelength.

By comparing the results from the above graphs, the addition of extra layers does not significantly affect the width of the zone of high reflectance but increases the reflectance within it and the sharpness of oscillations outside.

2. Materials and methods

2.1. Description of reflection / transmission UV- vis spectrometer set-up.

2.1.1. Equipment used in this set-up

The main equipments used in this set-up are:

- CM110 Monochromator,
- White light source,
- AD130 photodetector Module and,
- LABVIEW program to control the CM110 and the AD130.

The CM110 specifications [23] can be summarised as follows:

- Focal length: 110mm
- Beam path: Straight through standard, right angle provided on request.
- Wavelength accuracy: ± 0.2nm
- Slits: Standard, ranges from 0 to 1 mm.
- Max Resolution: 0.2nm / mm grating.

The AD130 detector is also a computer-controlled data acquisition device, which is used in conjunction with the monochromator CM110 for spectroscopic applications. It also covers a wide wavelength range with Ge, PbS, and PbSe photocells [23].

2.1.2. Controlling the CM110 and the AD130 with LABVIEW.

In order to control and plot the data coming from the CM110 and AD130 software, a graphical programming language called LABVIEW was introduced to manipulate the data. The CM110 and the AD130 can communicate very easily with the LABVIEW program, where the control electronics and calibration can occur automatically in each instrument.

(α) Description of reflection set-up

The main objective of using the reflection set-up in this project is to analyse the deposited thin films obtained using the vacuum evaporation system. Basically, this reflection set-up is like a Michelson interferometer [24-26]. Its configuration is illustrated in figure 2.1.

When a beam of light passes through the beamsplitter, it divides into two. One segment travelling along the reference arm, to the left, and the other one into the sample arm.

To use this reflection set-up, and before taking any spectrum of any sample, we need to make sure that the apparatus is aligned and operating properly. This will require:

(i) Calibration of the monochromator in order to obtain a good resolution while running spectra.

Good resolution, which can be achieved by using suitable slits at the entrance and the output of the monochromator.

(ii) Good alignment of the beam throughout the set-up.

Once everything is ready to run, two signals (background (BS) and reference (refS)) are recorded first in order to set the LABVIEW program ready to record the actual reflection signal. The blocks are inserted to stop the light from getting through to the sample or the reference mirror. These signals were taken as follow:

- Background signal - where two blocks are inserted between the beamsplitter and the sample arm from one side and between the beamsplitter and the reference arm from the other side.
- Reference signal - where the block is inserted between the sample arm and the beamsplitter.
- Finally, a reflection signal (RS) is obtained once the block is inserted between the reference mirror and the beamsplitter.

The data of the (BS) and (refS) were first stored in a directory within Labview program, and the actual reflection signal was then generated using the formula [37]:

Actual reflection signal = (RS – BS) / (refS – BS)

A schematic diagram of the reflection set-up is shown below.

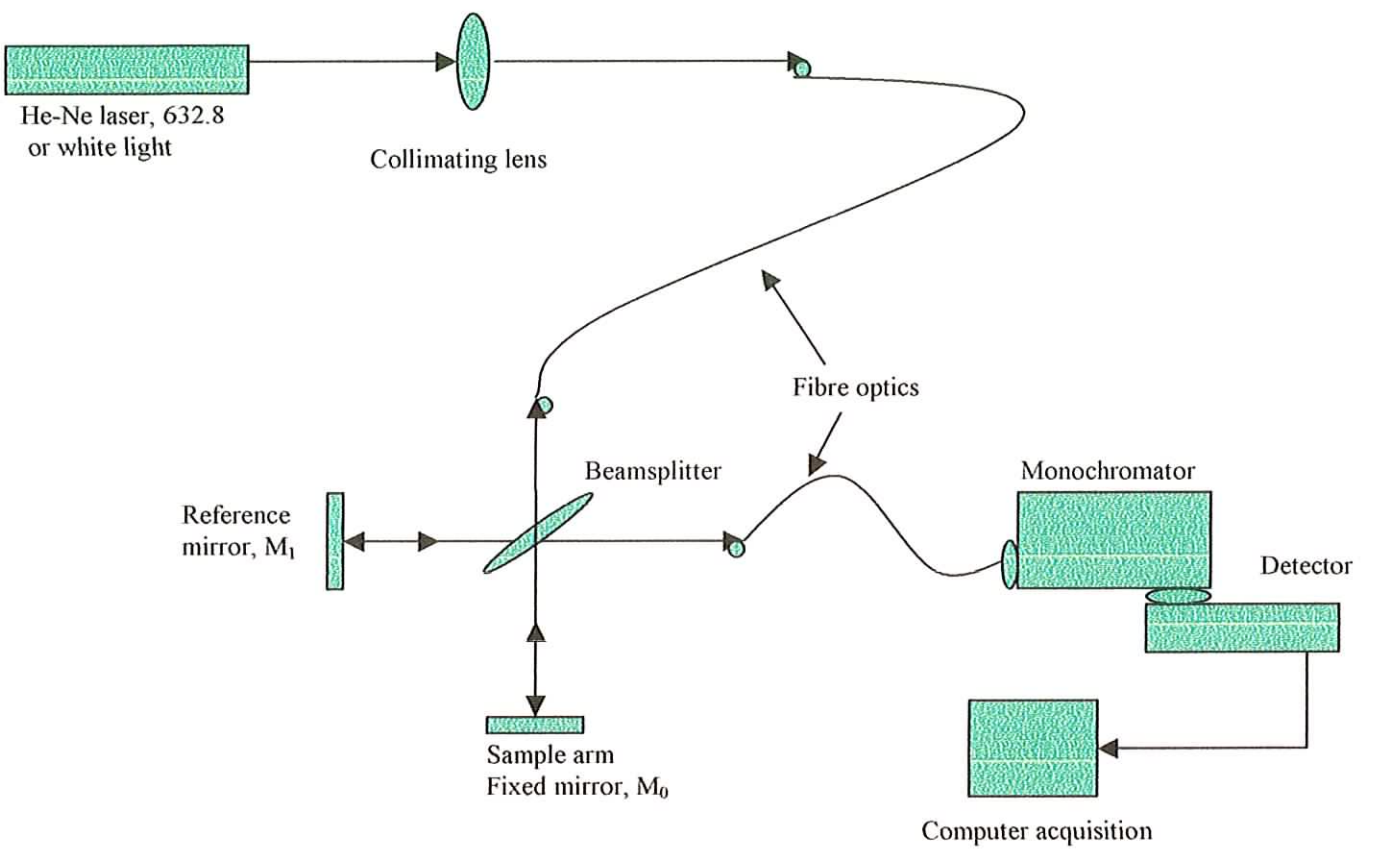

Fig.2.1. Reflectometer measurement system.

(β) Transmission set-up

The transmission set-up is very straightforward. Once the apparatus has been aligned as in the previous reflection set up (omitting the reflection components - beamsplitter and

mirrors), the sample is placed between the light source and the monochromator. Now the sample can be characterised spectroscopically as in the previous set up. The transmission set up is illustrated below in figure 2.2.

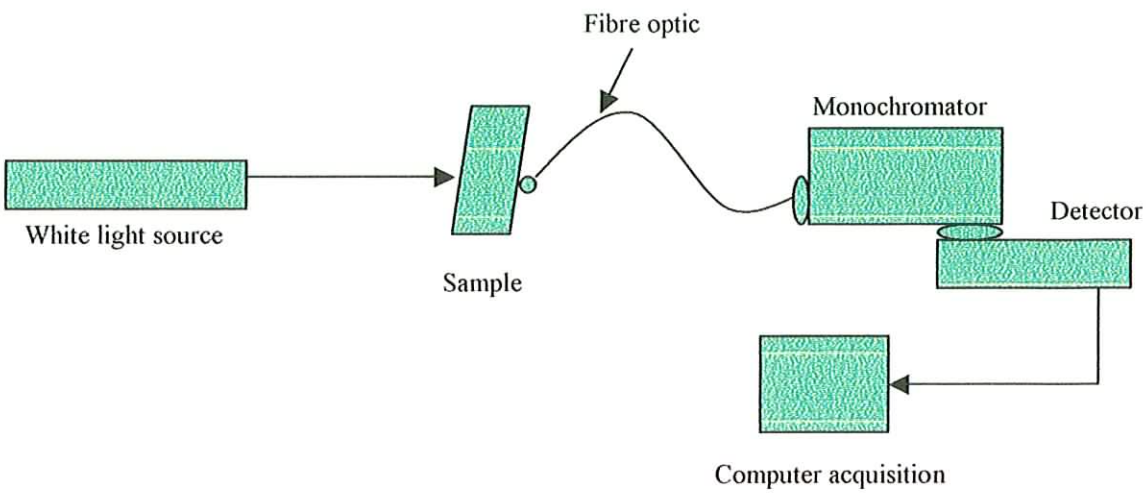

Fig.2.2. Transmission set up diagram.

The transmission spectrum for each individual deposited film can be obtained with the same way as described for the reflection set up. Where a background and reference spectra were taken first, then a transmission spectrum is obtained. The resultant spectrum will be compared first to the one obtained from the UV- vis spectrometer. This will allow us to choose the most accurate technique with higher resolution for any further characterisation. Finally modelling of these structures will be carried out for comparison with our measured results.

2.2. Description of vacuum evaporation technique

In this section, a brief description is given regarding how vacuum evaporation is used in the production of thin-film filters. But first of all we need to outline the basic process involved in the vacuum evaporation technique.

As fully described in Holland and Macleod textbooks, there are different deposition techniques for preparing thin solid films [27,28]:

- Electro-deposition.
- Chemical precipitation.
- Cathodic sputtering.
- Vacuum evaporation, etc.

However, modern thin-film optical filters are almost entirely manufactured by the process of vacuum evaporation.

If a small amount of material that is solid at room temperature is heated in air, providing it does not decompose or react with its surroundings, it will eventually vaporise. Any cold surface near the source will become coated with the material but the deposit will be extremely powdery and porous, and is unlikely to possess any useful optical properties [29]. If the heating is carried out in vacuum, the situation is quite different. Firstly, any reaction with the atmosphere is negligible, provided the residual gases in the chamber are at a sufficiently low pressure, and secondly, the molecules appear to travel in straight lines.

If a substrate, which is cold relative to the melting point of the material, is introduced into the vapour stream, a solid deposit will build up on it with properties broadly similar to those of the original bulk starting material, provided certain precautions are taken. The issue of the quality of the deposited film is subject to some predetermined conditions, such as substrate heating, pressure and rate of evaporation. The evaporation is carried out in a sealed chamber that is exhausted to a pressure usually of the order of 10^{-5} torr [30,32].

The materials to be deposited, or evaporated, are generally melted in refractory crucibles, which are heated electrically.

The complete plant consists of the chamber together with the necessary pumps, pressure gauges, power supplies for the crucible heaters, substrate- holding jigs, substrate heaters and the controls given that the crucible material does not decompose at the evaporation temperature of the material to be evaporated. There are two main factors that govern the choice of crucible and heating method. The first is the evaporation temperature itself, and the second is the tendency of the evaporant to react with the crucible material. By far the simplest and most common method is to make use of a boat of refractory metal which performs the dual function of crucible and, when an electric current is passed through it, of heater. Typically, we used Molybdenum metal boats in this project because its evaporation temperature is very high 2100 ^{0}C [33].

Figure 2.3, shows a schematic diagram of the main features of the vacuum evaporation inside a vacuum chamber. The cleaning and evaporation process involved in a typical coating is described carefully in the next section.

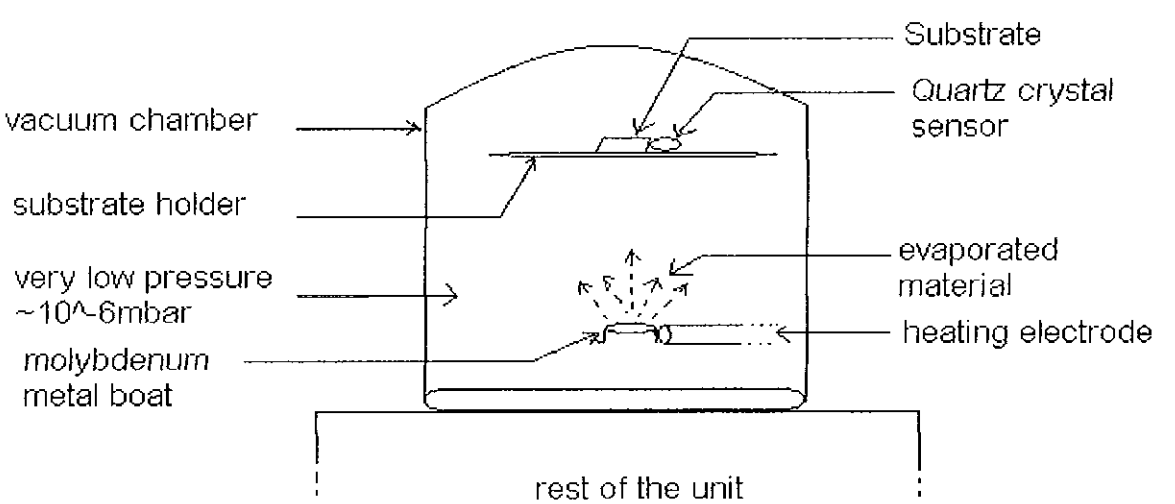

Fig.2.3. Schematic diagram of the main features of the vacuum chamber.

A picture of the Edwards Auto Evaporation System used in these experiments is shown below in order to give the reader the latest shape of the unit since first introduced in 1956.

More historical information about this vacuum evaporator unit is laid out in both textbooks by Holland and Macleod [27,28].

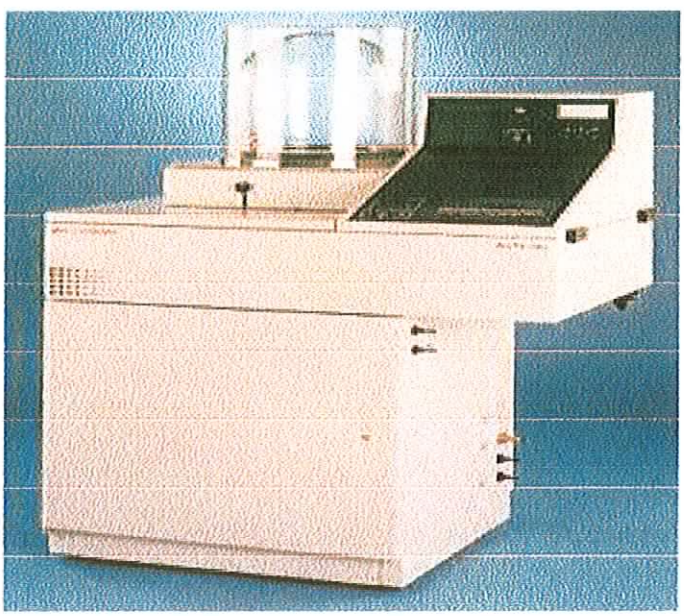

Fig.2.4. Photograph of the Auto 306 Vacuum coater, downloaded from the manufacturing company web site " www.boc.com/evt/products/tfd", (2000).

3. Growth and characterisation of single-layered structures.

3.1. How to deposit thin film layers on a glass substrate, e.g. Zinc Sulfide.

The deposition of dielectric films that have maximum environmental stability and transparency is the ultimate desire of the vacuum coater. The standard techniques of physical vapour deposition can approach the ultimate properties to a high degree if all of the evaporation/ deposition parameters are optimum. These include:

- Starting material form, purity and composition;
- Substrate temperature and surface condition;
- Chamber pressure, evaporation rate;
- Evaporation technique.

Some thin films have been produced using the Auto 306 Vacuum coater described in the previous chapter.

The process of deposition can be described as follows:

(i) Starting material: Zinc Sulfide, ZnS (99.9 % purity). The refractive index of ZnS is taken to be 2.36.

(ii) Substrate cleaning: there are different methods for cleaning substrates before the evaporation process starts. The following cleaning procedure was found to work well:

- Rinse the slide with acetone, then place it in a beaker of acetone, in the ultra- sonic bath for 10 minutes.
- Remove slide and place it in a beaker of methanol, then back into the ultra- sonic bath for another 10 minutes.

- Remove from bath and quickly rinse again with acetone (acetone evaporates more easily and prevents watermarks forming on the slide).
- Dry the slide as quickly as possible using a hairdryer. If dust or any watermarks remain rinse in acetone again and dry quickly.

(iii) Substrate heaters of the vacuum evaporator are generally used to provide the energy needed to promote film growth to a higher quality. These temperatures create a high surface mobility for the arriving molecules, which is necessary to ensure a dense microstructure growth and thus stable layers, although in this work we found it did not play a major role.

(iv) The specification of the Auto 306 vacuum coater with regard to the chamber pressure indicates that before growing any film, the chamber pressure has to be dropped to around 4×10^{-6} mbar. This low pressure can be achieved very quickly by adding liquid Nitrogen to the liquid Nitrogen trap, to aid main rotary back diffusion.

The rate of evaporation deposition is important for the film quality. If the rate of deposition is too great, the condensate molecules will not have sufficient time to restructure into a good film. This less dense film is thus susceptible to strain changes that can lead to fading and cracking.

Consequently a medium rate of evaporation and a substrate heating temperature (above 250 ^{0}C) can promote the densification of the growing film.

(v) The process of evaporation of ZnS using the vacuum coater, can be carried out as follows:

- Turn the cooling-water supply on and then press the start button.
- Wait 15 minutes for the machine to warm up. The controller display will show 'SEALED' and then press 'VENT' to vent the chamber.
- Open the vacuum chamber and load the substrate that is a 76×26mm microscopic glass slide, and the material to be evaporated. The substrate must be positioned directly over the boat, otherwise it will result in non-uniform deposition across the slide.
- Close the chamber and press 'CYCLE' button for the pumping system to start to reduce the chamber pressure. The following displays will be shown on the top line of the controller display in sequence to indicate that the pressure inside the chamber is decreasing.

  (i) Roughing

  (ii) Pumping

  (iii) Fine-pumping.

- Use of liquid Nitrogen may be introduced in order to achieve low pressure in a very short of time. Approximately 1.4 litre of liquid N_2 can be supplied into the liquid nitrogen trap before the pumping process starts; and can be sufficient for up to eight hours of cryopumping.

Once the chamber pressure reaches 6. 10^{-6} mbar roughly, while the shield is in place (to protect the substrate from impurities), the current is increased until the boat just starts to visibly glow (note: this will occur at different currents for different boats and masses used).

The pressure should rise slightly and then start to fall again. Turn the current off after about 1 minute. Wait for the pressure to reach around 4.10^{-6} mbar, then turn the current up as before. If the pressure increases by a relatively large amount, it means there is an outgassing problem, which will probably affect the cleanliness of the slide and therefore, film quality and thickness. After about 1 minute, the shield can be removed and deposition started. A medium rate of evaporation should be maintained all the time in order to allow a uniform condensation of ZnS molecules on the substrate.

Finally, once the film has been deposited, and when all the ZnS pieces have been evaporated, the chamber should be allowed to cool down for about 20 minutes. This is necessary to prevent any formation of carbon dioxide inside the chamber. So approximately 20 minutes is needed to cool the chamber such that it can be vented and the film can be removed.

3.2. Properties of ZnS pieces [34]

- Material form: pieces
- Purity: 99.9 %
- Transparent region: 0.6-16 μm
- Refractive index: 2.35 - 2.6
- Evaporation temperature: 800 ^{0}C
- Density: 3.8 gm/cc.

3.3. Characterisation of the deposited thin film layers of ZnS

3.3.1. Measuring the thickness of each film using DEKTAK.

DEKTAK is a very high precision STYLUS measurement instrument capable of measuring the thickness of thin films. It is comprised of three main components:

1. Scan head,
2. Monitor attached to a camera for visualising the sample, and
3. Computer acquisition.

Figure 3.1 shows a picture of the scan head and the monitor, where figure 3.2 shows how the thickness of a film can be measured using a stylus [35].

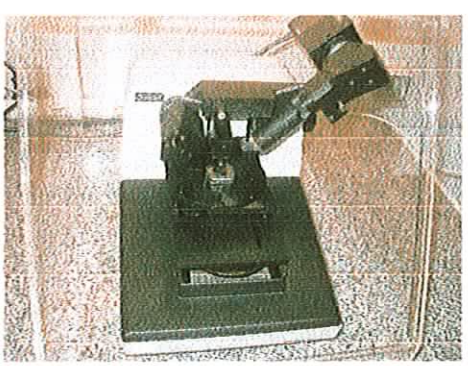

Fig.3.1. Photograph of DEKTAK instrument for measuring the thickness of thin films.

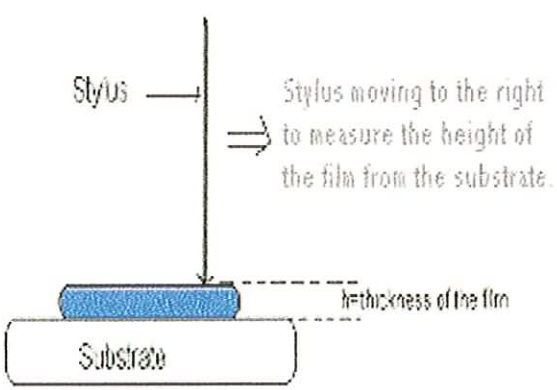

Fig.3.2. Schematic diagram of a stylus profilometry measurement

(α) How to measure the thickness of a thin film using Dektak

Place the sample on the sample stage and position it for scanning using the stage translation, rotation and levelling controls. The DEKTAK allows manual sample positioning via precision thumbwheel controls. Dual repositionable crosshair reticules are displayed on the monitor to aid in stylus and sample positioning.

When a scan is run the stylus is lowered onto the sample surface, and the stage moves the sample as the stylus rides over the surface features. The video monitor will allow you to view both the physical scanning of the sample and the plotting of the data simultaneously. At the end of the scan, the stylus automatically retracts and the system is immediately ready for the next scan bearing in mind that the DEKTAK precision is about 1 A^0.

The surface features encountered by the stylus are represented as a two-dimensional profile, which is plotted, scaled, and displayed on a video monitor [35].

• *Examples*

Let' s take three deposited single layers of Zinc Sulfide. The thickness of each deposited layer and the mass of the evaporated ZnS are tabulated in table 1.

Thin-films of ZnS	Number of layers	Mass of the evaporated ZnS (mg)	Thickness of the formed layer (nm)
Sample 1	1	9.1	50-70
Sample 2	1	70.4	380-460
Sample 3	1	132.2	820-980

Table 1. Measuring the thickness of each deposited layer of ZnS using DEKTAK.

As expected, the deposited layer of Zinc Sulfide wasn't uniform along the substrate. Even though, the thickness of the formed layer of ZnS on the substrate wasn't uniform. However the layer's thickness seems to be linear along some parts of the slide. These preliminarily results will be explained more carefully once the modelling of these structures is carried out (next chapter).

3.3.2. Measuring the thickness of each thin-film using Phase-Contrast Microscope

The phase-contrast microscope used in this project is a noncontact three-dimensional optical profiler for measuring thickness [50,51]. The system in general relies on the principle of a Michelson interferometer, where the surface of the sample replaces one of the mirrors.

Figure 3.3 shows a photograph of the Phase-Contrast Microscope system connected to a desktop computer. Figure 3.4 shows a schematic diagram of a multiple beam reflection set up of the instrument, which is normally called a Mirau interferometer [52].

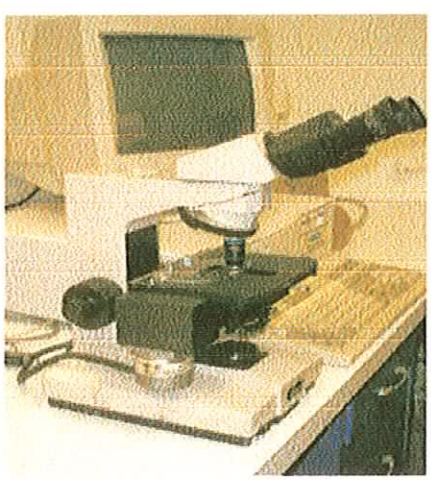

Fig.3.3. Photograph of the phase-contrast microscope downloaded from the web site "www.emsl.com".

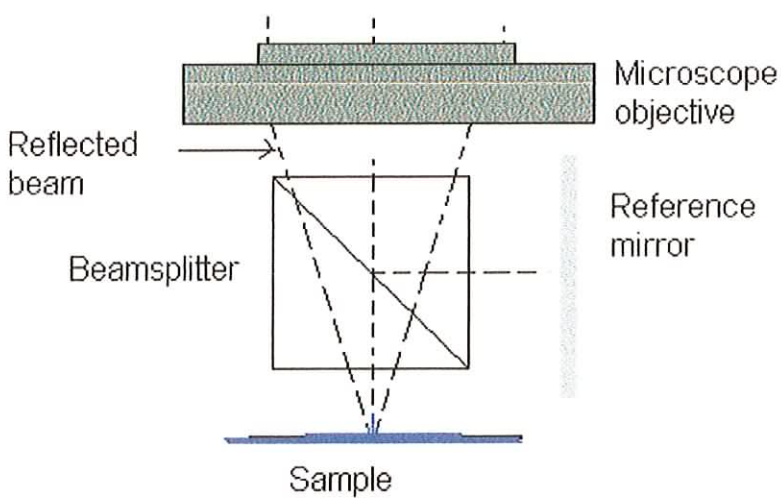

Fig.3.4. Schematic diagram of the Mirau interferometer

The diagram in figure 3.4 can be described as follows:

A light beam of short coherence length is split into two parts by a beamsplitter so as to illuminate both the surface and a reference mirror. On recombination of the beams at the beamsplitter, interference effects are obtained only if the optical path difference in the

interferometer is less than the coherence length. As the mirror is translated, a CCD camera images the surface and passes it to a PC. As the path length of the reference beam changes, different regions of the objects surface meet the coherence condition and the light intensity at the corresponding CCD pixels is modulated. By noting where the reference mirror is when each pixel is modulated a profile of the surface can be progressively built up.

The technique is non-contact and covers the whole surface, unlike the conventional stylus profilometry of the Dektak.

- *Example*

By using the phase-contrast microscope and trying to measure the thickness of a deposited thin film, the results show that it is impossible to measure the thickness of a very thin film (less than 60 nm thick) or a very thick film (greater than 800 nm). However, a test was carried out for a film whose thickness was measured by the Dektak as 160 nm.

Below is an image of the surface of a deposited thin film of ZnS, where the Phase Contrast microscope is used to measure the thickness of the film.

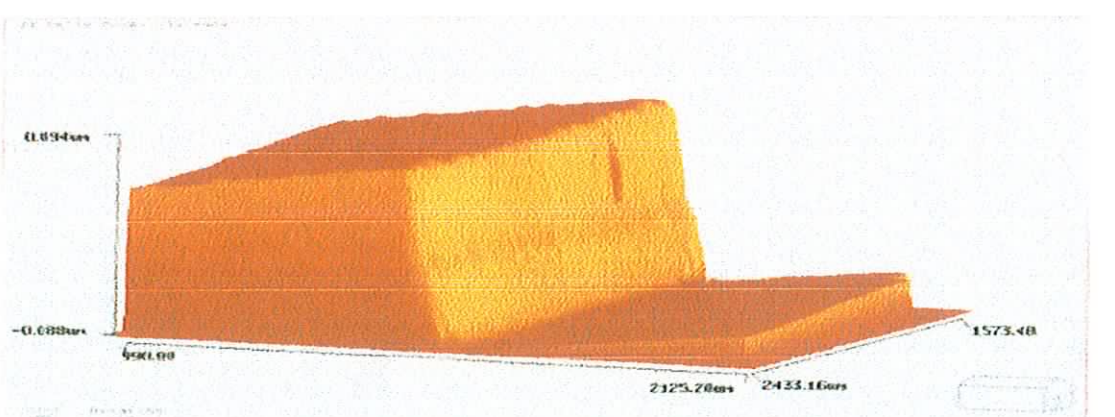

Fig.3.5. Image of the surface of a deposited layer of ZnS, obtained using the phase-contrast microscope.

The height of the step is measured to be 157 nm after several attempts. This result was confirmed, for the same slide, with the Dektak measurement.

Because the Dektak is very easy to manipulate, and has a greater range and good resolution, it was decided to use only the Dektak.

3.3.3. Specification of the Perkin Elmer UV/VIS/NIR Spectrometer

The Perkin Elmer Lambda 900 UV/VIS/NIR Spectrometer used to characterise thin films, is an automated spectrometer with a higher resolution than that obtained using the CM110.

Some of the features of the UV/VIS Spectrometer [36] are outlined as follows:

- It is a double beam (i.e. reference and sample beams) instrument.
- Double monochromator with pre-aligned tungsten-halogen and deuterium lamps as sources.
- The wavelength range is -175 – 3300 nm.
- Accuracy: - 0.08nm in the UV-visible region.
  - 0.3nm in the NIR region

3.3.4. UV-vis spectra of the three samples, using the Perkin-Elmer.

In order to characterise thin-films spectroscopically, we intended to run some UV-vis spectra of each film using the Perkin Elmer. Figure 3.6 represents the transmission of each deposited film as a function of wavelength.

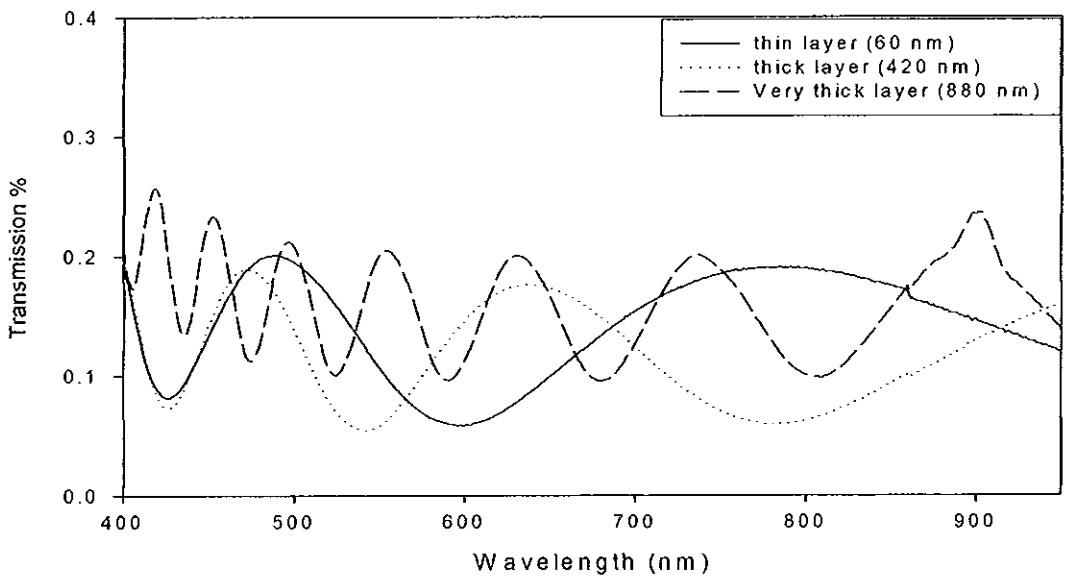

Fig.3.6. Transmission spectra of the grown samples of Zinc Sulfide as a function of wavelength using the Perkin Elmer UV-vis interferometer.

The solid, dotted and dashed graphs represent the UV vis transmission spectra of thin (60 nm), thick (420 nm) and very thick (880 nm) layers of ZnS respectively, deposited on a glass substrate.

The first investigation of these UV-vis graphs, shown above in figure 3.6, shows that there is a relationship between the thickness of the layer and the spacing of the maxima. The thicker the layer the closer the spacing of the maxima. The curve's oscillations are due to interferences of multiple reflections.

For further characterisation of the same samples we used the CM110 to get transmission spectra of the three samples. This technique was used mainly to compare the resolution of the UV-vis spectrometer and that of the CM110.

3.3.5. Transmission spectra of the three samples, using the CM110.

As mentioned already in section (2.1), the transmission spectrum of each prepared sample can be carried out as described in Fig.2.2.

The following transmission spectra were obtained for each sample

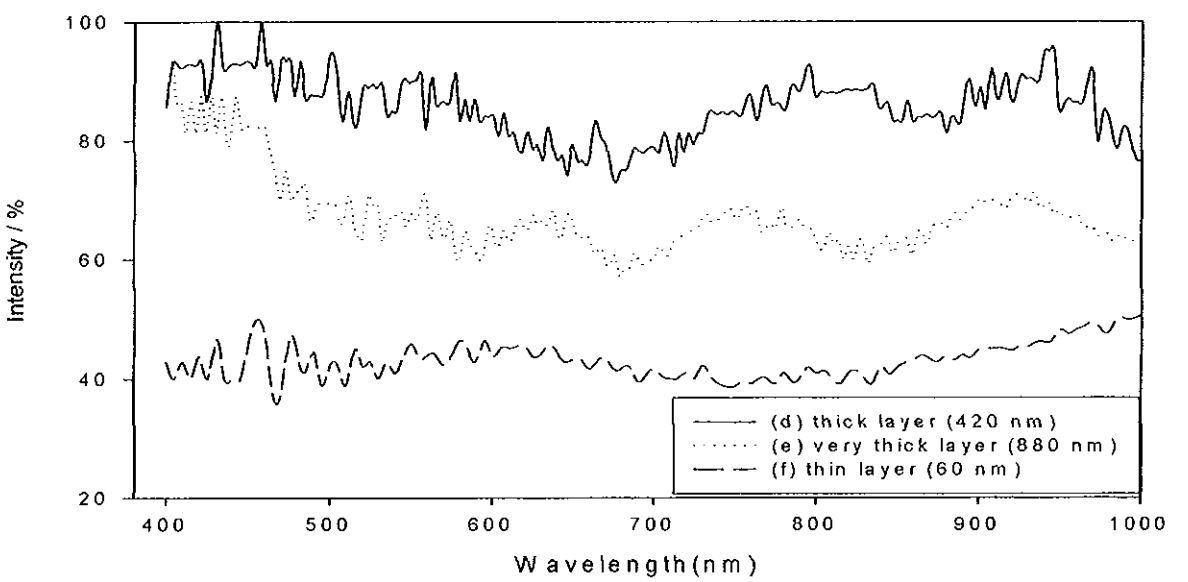

Fig.3.7. Transmission spectra of the grown samples of Zinc Sulfide as a function of wavelength using the CM110.

Graphs (d), (e) and (f) represent the transmission spectra of the same samples used earlier (thin, thick and very thick layers of ZnS) to be characterised, using the CM110.

Figure 3.7, shows that the spectral measurements of the CM 110 are quite different from the one obtained using the Perkin-Elmer UV-Vis, shown in figure 3.6. This is obvious when comparing the intensity and the number of oscillations shown on each graph for the same sample.

The thicker the layer, the more oscillations will take place. The analysis of these spectra shows as well lack of smoothness of each spectrum. This roughness can be improved only by increasing the 'sample averaging' of the LBVIEW program.

However, all the spectra obtained using the Perkin-Elmer or the CM110 of each particular sample do not match fully. This was expected, since the resolution of the Perkin-Elmer instrument is far better than the CM110. The next stage is modelling these thin films.

4. Modelling the grown single-layer films

A computer program as described earlier in section 1.3 which is run in Matlab, runs a control window (Appendices B1, B2 and B3), which allows the input of parameters and choices for the calculations and the plots required for any structure such as transmission and reflection. Once all the parameters of the structure to be modelled are defined, the results are automatically plotted on completion of the calculations [37].

At this stage it is assumed the refractive index of ZnS is constant at the scanning wavelength (350-950 nm). Dispersion will be incorporated later. By varying the thickness parameter and trying to match the best-fit curve to the one obtained by UV-vis, we are able to model the correct thickness for each individual structure. Figures 4.1, 4.2 and 4.3 show the predicted spectrum and thickness for each individual deposited thin film of ZnS.

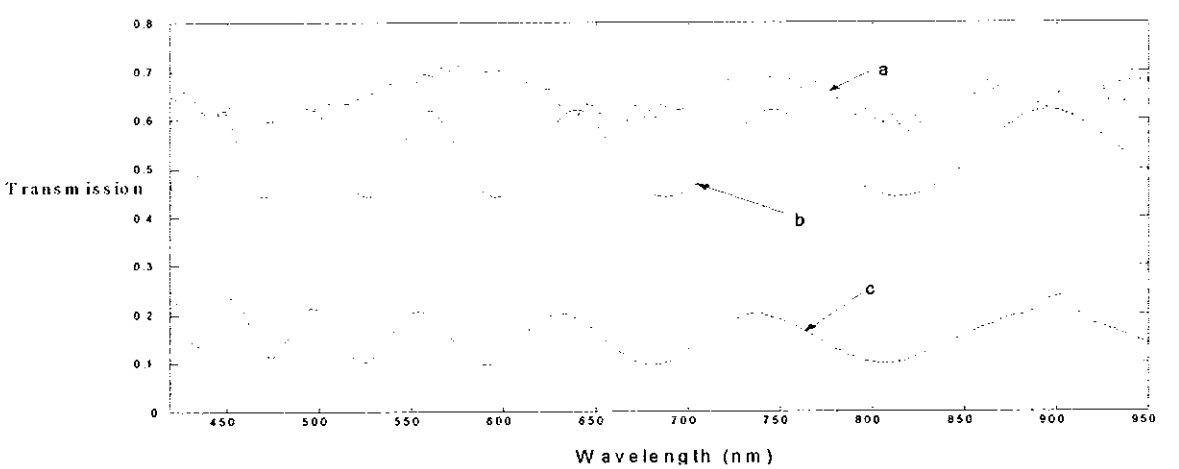

Fig.4.1. Matching the UV-vis transmission spectrum with the modelled spectrum to predict the actual thickness of a very thick grown single layer of zinc sulphide where a, b and c spectra were obtained using the CM110, MATLAB and the Perkin Elmer respectively.

As shown in figure 4.1, spectrum (a) does not match the other spectra (b) and (c). On the other hand, the modelling results (spectrum b) agrees with the Perkin-Elmer data

(spectrum c). This is because the resolution of the CM110 is very weak in comparison to that of the Perkin-Elmer and the model is always higher than experimental results.

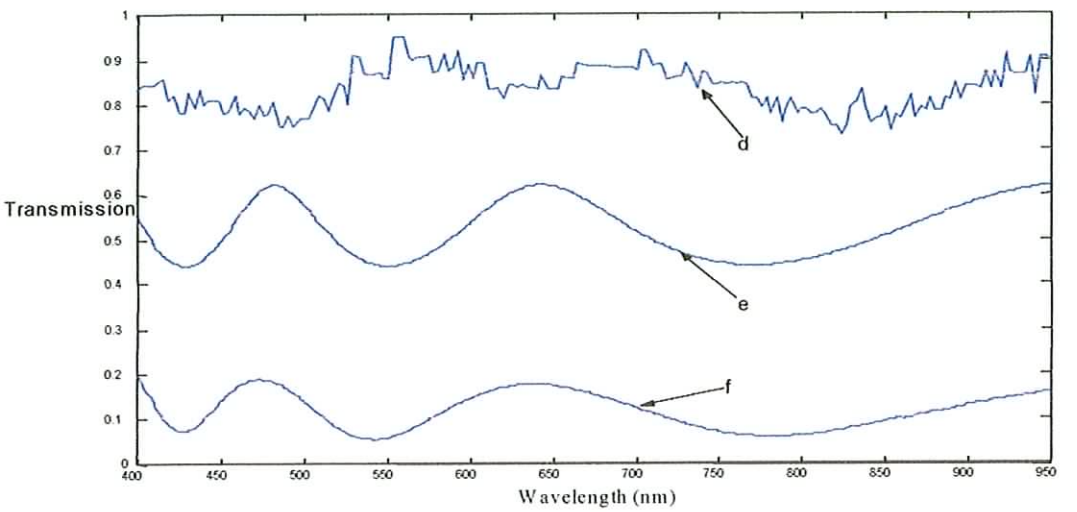

Fig.4.2. Matching the UV-vis transmission spectrum with the modelled spectrum to predict the actual thickness of a thick grown single layer of zinc sulfide where d, e and f spectra were obtained using the CM110, Matlab and the Perkin-Elmer respectively.

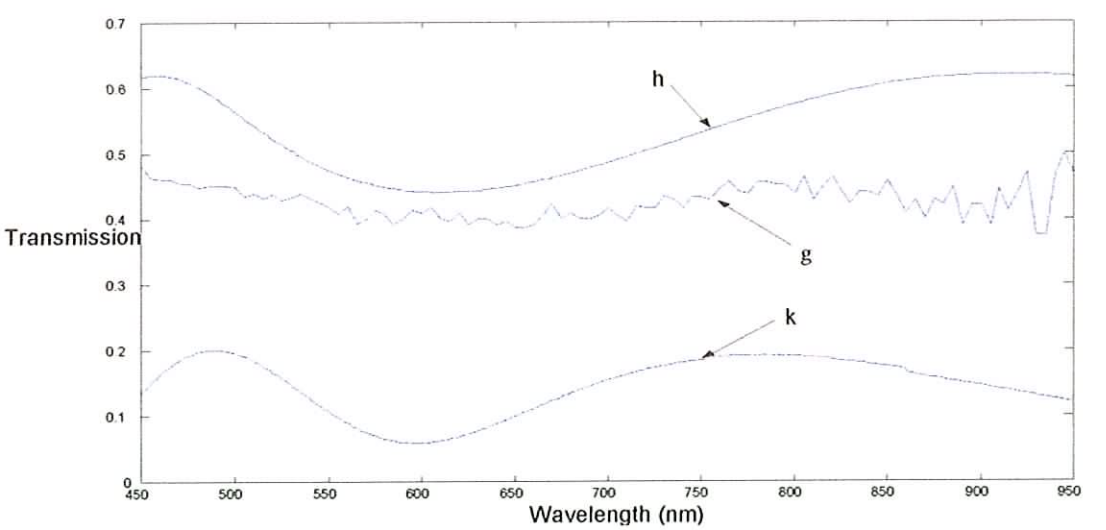

Fig.4.3. Matching the UV-vis transmission spectrum with the modelled spectrum to predict the actual thickness of a thin grown single layer of zinc sulphide where g, h and k spectra were obtained using the CM110, Matlab and the Perkin-Elmer respectively.

In order to model these samples and to get the predicted thickness using MATLAB, the layer thickness parameter is varied until the spectral features in the calculated spectrum matches those in the measured spectrum.

In figure 4.1, by fitting only for thickness into the program, it was found that the thickness that will give a spectrum similar to the one obtained using UV-Vis and CM110 is

d= 50 nm. This result was already obtained using DEKTAK, which confirmed it to be between 50-70 nm.

This is also true for figure 4.2 where the refractive index was maintained constant over the region of scanning, the thickness of the second thin film of ZnS was found to be: d = 408 nm. This result was also obtained earlier, where DEKTAK measurements states something similar, '380-460 nm'.

The thickness of the third thin film, figure 4.3, obtained from the modelling was d = 955 nm. This thickness was also confirmed using DEKTAK as 820-980 nm.

5. Growth and characterisation of multilayer structures of ZnS and MgF_2.

5.1. Properties of MgF_2 pieces

The second dielectric material, which was used to make a multilayer structure, is magnesium fluoride, MgF_2. Its properties [34] are as follows:

- Material form: pieces
- Purity: 99.99 %
- Refractive index: 1.37 – 1.38 (in the visible region)
- Evaporation temperature: 950 ^{0}C
- Transparent region: 0.12-7 μm
- Substrate temperature: 250 °C
- Density: 3.18 gm/cc

5.2. Making multilayer structures of ZnS and MgF_2

The deposition procedure outlined in chapter 2 for a single layer, was applied with the same way to the growth of a multilayer film of ZnS and MgF_2.

As stated before, the main goal of the experimental work of this project is to investigate the optical properties of a multilayer dielectric Fabry-Perot cavity with a birefringent material, experimentally and theoretically. For this reason we need to grow a high reflectivity Distributed Bragg Reflector (DBR) to form the mirrors of the Fabry-Perot cavity.

A simple DBR consists of multiple layers of alternating high-and low-index materials arranged periodically. The thickness of each layer is chosen so as to satisfy the Bragg quarter-wave condition: $d = \frac{\lambda_0}{4n}$

where λ_0 is the reference wavelength of the structure, and d and n are the thickness and the real part of the linear refractive index of a particular layer, respectively.

To prepare these kinds of dielectric mirrors under the predefined conditions described above, we used dual sources in the vacuum evaporator, one for Zinc sulfide and the other one for Magnesium fluoride.

Before starting deposition of the DBR, some precautions need to be taken and parameters to be chosen as reference for a successful evaporation:

- Cleaning process: cleaning the substrate and the boat must be carried out in the manner described in chapter 2.
- Reference wavelength of the structure was chosen to be $\lambda_0 = 600$ nm for simplicity.
- At $\lambda_0 = 600$ nm, the refractive indices of ZnS and MgF_2 are 2.36 and 1.38 respectively [34]. Therefore the desired layer thicknesses ($d = \frac{\lambda_0}{4n}$) are 64 and 109 nm for ZnS and MgF_2 respectively.
- Measuring the deposited layer thickness: the layer thicknesses were measured in situ by a quartz crystal thickness monitor [31]. Its accuracy does not reach the expected results, because its spectral resolution is weak for such measurements, especially when measuring very thin thicknesses. Moreover, the lifetime of the quartz crystal sensor is very short before starting to give inadequate measurements. These inconveniences

will definitely affect our results, and the only way around it is to ultimately rely on model fitting.

- The substrate heater: the substrate, which is a microscope glass slide, was not temperature controlled during the growth [32]. After a few runs, with the substrate heater on, it was found that nothing was deposited on the substrate. Once the deposition was carried out without it, good mirrors were obtained again.
- Deposition rate: the deposition rate for this kind of dielectric multilayer film was controlled at about 0.1~0.2 nm/s, with a maximum current through the boat of about 40 Amps.

All these precautions were taken into account and mirrors were grown. Various mirrors with different odd numbers of layers and with a ZnS layer on top (ZnS is more robust and not easily affected by air as MgF_2) were deposited for characterisation.

5.3. Transmission spectra of the grown multilayer structures

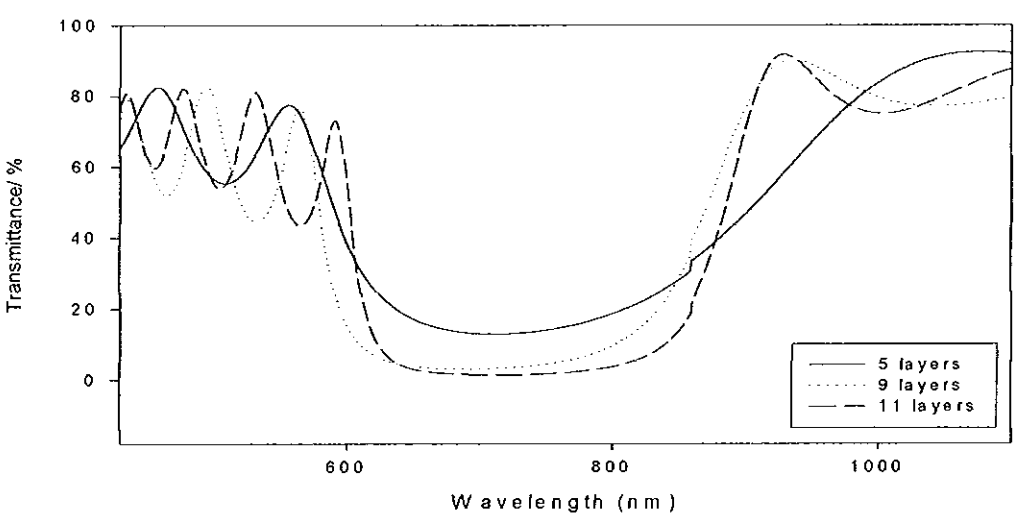

Fig.5.1. Measured transmittance (using the UV-vis spectrometer) for normal incidence of alternating $\lambda_0/4$ layers of high-(n_{ZnS}=2.36) and low-index (n_{MgF2}=1.38) on a glass substrate as a function of the wavelength for λ_0 =600 nm. The number of layers is shown for each curve.

Figure 5.1 shows the variations of transmittance of three grown quarter-wave stacks of alternating layers (5, 9 and 11-layers) of zinc sulfide and magnesium fluoride.

The characteristics of these spectra show the expected behaviour of a typical quarter-wave stack that is:

- The low-transmission zone can be seen to be limited in extent.
- Addition of extra layers does not affect the width of the zone of low transmittance but increases the number of oscillations outside the low transmission.

However, the measured transmission spectra are shifted to the longer wavelength, and not centred at the monitoring wavelength (λ_0 =600 nm) as was expected.

This result can only be explained by assuming that the actual thickness of each grown layer is bigger than what was indicated by the quartz crystal sensor thickness monitor

6. Modelling grown multilayer structures with dispersion.

6.1. Dispersion of refractive index for ZnS and MgF_2.

So far, we have used only a single value for the real part of the refractive index for each evaporated material and neglected the imaginary part, which is directly related to absorption. In fact, the refractive index of a material is not constant for light of different wavelengths [38,39].

Therefore in order to model, with a higher accuracy, any grown test structure (single or multilayer), we need to include this dispersion of the refractive index in our modelling.

To do so, the programme was expanded to express the complex index of refraction for each material (ZnS and MgF_2) as a function of wavelength. In general the index of refraction for a material can be written as a complex form: $n = n_R + in_I$ [20].

Initially the experimental data of refractive index against wavelength of ZnS and MgF_2 were obtained from material suppliers and then the real part and the imaginary parts of the refractive index of each material were expressed as a function of wavelength, by carrying out the calculations described in Appendix C [40].

(i) Zinc sulfide.

Plots of the measured refractive index and absorption coefficient against wavelength for zinc sulfide are shown below [40, 41].

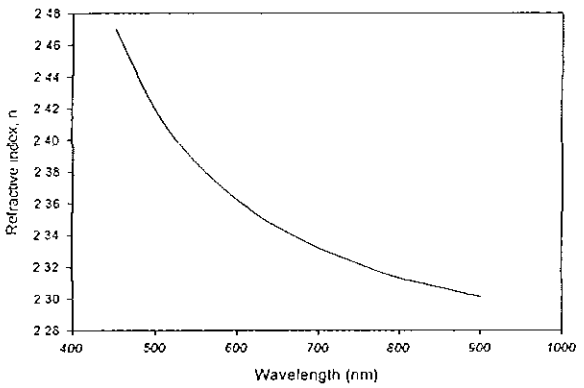

Fig.6.1. Variation of refractive index of zinc sulfide against wavelength [40,41].

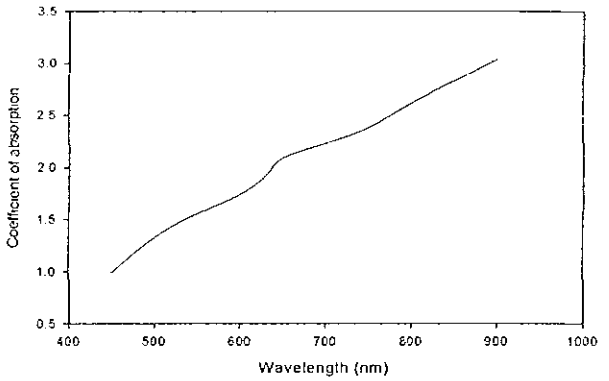

Fig.6.2. Coefficient of absorption versus wavelength for zinc sulfide [40,41].

Figures 6.1 and 6.2 show the variations of the real part of the refractive index and the absorption coefficient for zinc sulfide against wavelength respectively. The best-fit equation for each spectrum is laid out in Appendix C.

(ii) Magnesium fluoride.

In the same way, as for zinc sulfide, measured refractive indices data for magnesium fluoride [40,41] were collected and plots of the real part of the refractive index and the absorption coefficient against wavelength are shown below.

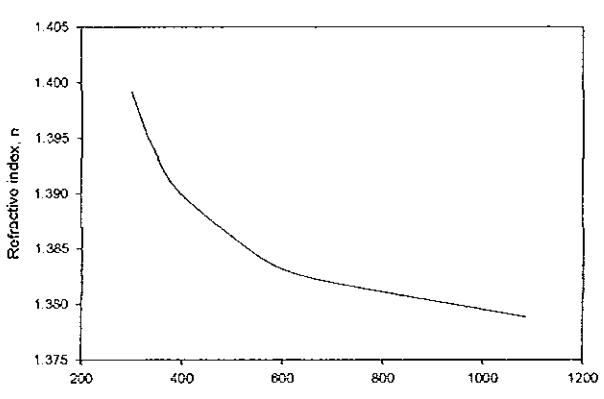

Fig.6.3. Variation of refractive index of magnesium fluoride against wavelength [40,41].

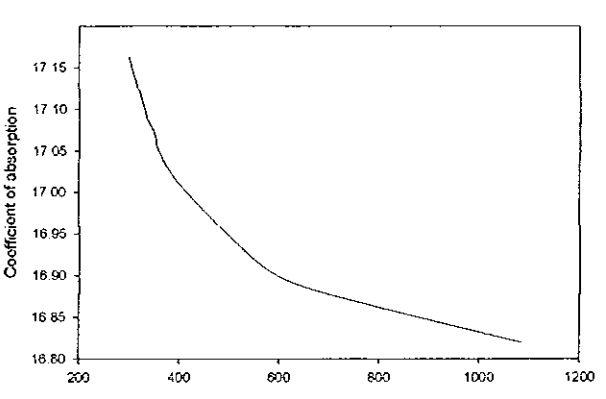

Fig. 6.4. Coefficient of absorption versus wavelength for magnesium fluoride [40,41].

Theoretical calculations of the reflectance, absorbance and coefficient of absorption for magnesium fluoride were carried out with the same way as for Zinc Sulfide. The equations that best fit the above spectra (figures 6.3 and 6.4) are listed in Appendix C.

Finally, we now have a wavelength dependent complex refractive index of zinc sulfide and magnesium fluoride, which will be used in any further calculation to include dispersion.

6.2. Modelling multilayer structure including dispersion, of a stack of alternating quarter-wave layers.

Figure 6.5 shows the modelled spectra of an eleven-layer quarter-wave stack of ZnS and MgF_2 with and without dispersion. When dispersion was included, a slight shift to the shorter wavelength was observed.

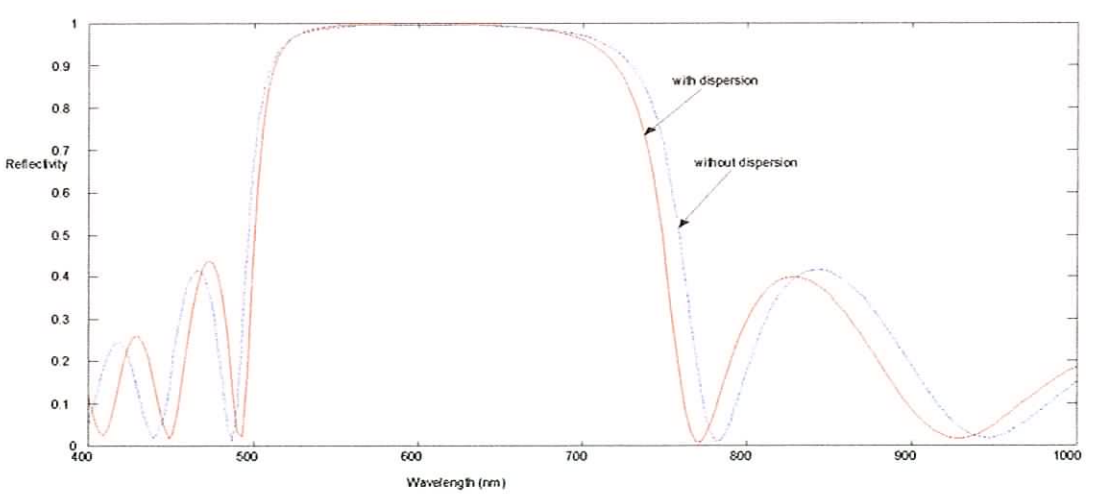

Fig.6.5. Modelling of an eleven-layer quarter-wave stack of ZnS and MgF_2 with and without dispersion.

6.3. Modelling grown multi-layer quarter-wave stack of ZnS and MgF_2

As stated earlier, our Bragg mirror stacks were grown on glass substrates by using the vacuum evaporation technique. The mirrors consisted of alternating $\lambda/4$ layer pairs of two materials with different refractive indices, Zinc Sulfide and Magnesium Fluoride.

The indices of refraction at 600 nm are 2.36 and 1.38, and the quarter-wavelength layer thicknesses are 64 nm and 109 nm for ZnS and MgF_2, respectively. Mirrors were then grown to match the above Bragg conditions.

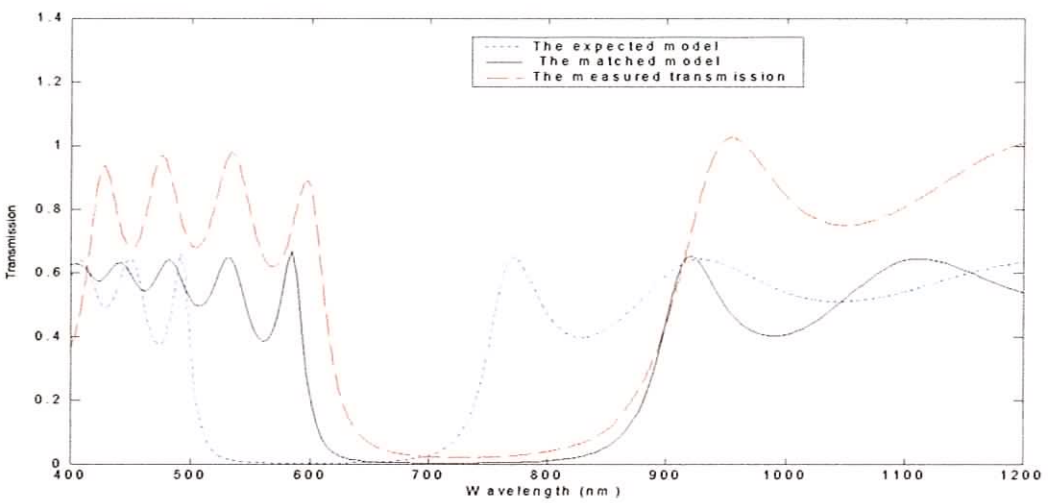

Fig.6.6. UV-Vis transmission spectrum (red dashed line) of an eleven-layer grown multilayer structure of ZnS and MgF_2 and its expected model (blue dotted line). The solid black line depicts the corresponding fits to the measurements.

Figure 6.6 depicts the UV-Vis transmission spectrum of a grown eleven-layer mirror of alternating ZnS and MgF_2, (red line), the fit according to the model, solid line (black), and the expected model according to theory using the above Bragg mirror conditions (blue).

The results shown in figure 6.6 indicate that there is not a full agreement between the measured transmission of the grown mirror (red dashed line), and the modelled transmission

using Matlab (blue line). The stop-band region of the grown mirror curve in figure 6.6, is shifted to longer wavelengths [42-43]. The grown eleven-layered dielectric multilayer structure of zinc sulfide and magnesium fluoride (in figure 6.6) exhibits a stop band from 670 nm to 820 nm with a corresponding reflectance of ~ 92 %, whereas the stop band of the model of the grown mirror lies between 520 nm and 680 nm, centred at 600 nm with a theoretical reflectance of 90% at 600 nm.

A systematic error occurred while measuring the thickness of each deposited layer on the glass substrate during growth using the quartz crystal sensor.

The shifted stop band of the grown mirror compared to that obtained from the modelling of the same structure indicates that the thicknesses of the grown layers are larger than expected.

In order to predict the thickness of each grown layer of Zinc Sulfide and Magnesium Fluoride, we modelled the measured transmission of the mirror with a corresponding fit curve as shown in figure 6.6 (black curve).

The design thickness of the layers was set to be:

	Expected thickness	Model fit	Ratio
Thickness(ZnS) (nm)	64	72	0.88
Thickness(MgF_2) (nm)	109	120	0.90

The results obtained from modelling the transmission of the grown film with the best corresponding fit indicate a systematic error of about an extra 11% on average on top of the expected thickness.

So the readings of the quartz-crystal sensor are not adequate and might be explained by the following reason: "the distance from the source to the substrate is smaller then the one to the quartz-crystal sensor", as shown below in figure 6.7. So more evaporant is deposited on the substrate than the thickness monitor is measuring (h2 is smaller than h1), where:

h1: is the travelling distance of the molecules from the source to the substrate.

h2: is the travelling distance of the molecules from the source to the quartz-crystal sensor.

In order to achieve an agreement between the experimental data and the modelling, calibration of the thickness monitor should be done, this will include:

- Implementing new quartz-crystal sensor for every deposition.
- Evaporation temperature, current supplied and the pressure inside the chamber should be fixed for a typical deposition.

All these parameters should be taken into account to estimate the difference in readings, which will be considered as an allowance for any subsequent depositions

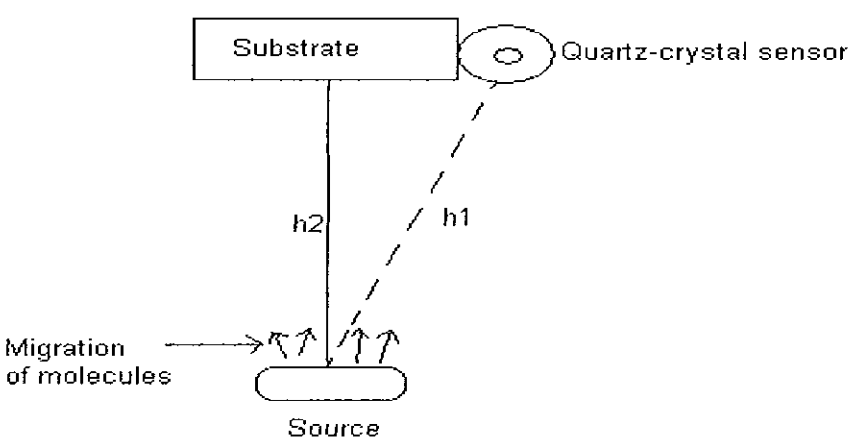

Fig.6.7. Diagram showing more molecules are deposited on the substrate than the quartz-crystal sensor is measuring.

7. Polarisation and Phase shift analysis in multilayer structures.

7.1. Definitions

In this chapter and before investigating the polarisation state of light in a multilayer structure, a summary of polarisation and birefringence is presented. The choice of quarter wave plates of quartz and PVA (polyvinyl alcohol film) as birefringent materials was selected for handiness. It is not easy to evaporate birefringent material using the vacuum evaporator to form a uniform layer and for this work we simply wanted proof of concept.

Light can be represented as a transverse electromagnetic wave made up of mutually perpendicular, oscillating electric and magnetic fields [20]. The left side of the following diagram shows the electric field in the xy plane, the magnetic field in the xz plane and the propagation of the wave in the x direction. The right half shows a line tracing out the electric field vector as it propagates.

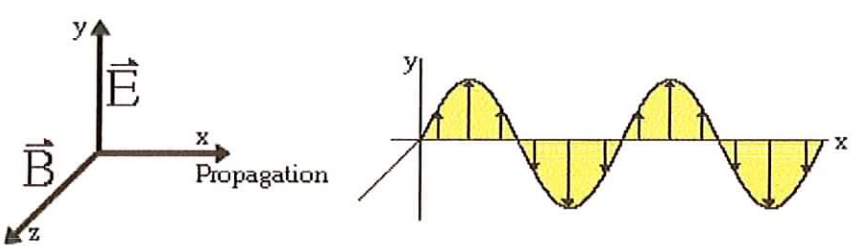

Fig.7.1. A schematic diagram of the magnetic and the E-fields vectors along a wave propagating along the x axis.

Light is considered to be "linearly polarised" when its two orthogonally polarised components fluctuate in one specific plane- the plane of polarisation and the components are

in phase. If it is elliptically polarised, the two components have a constant phase difference, and the tip of the electric field vector follows an elliptical shape as the beam propagates. Circularly polarised light is a special case of elliptically polarised light in which the two components have a 90° phase difference and the point of the electric field vector describes a circle. When viewed looking towards the source, a right circularly polarised beam has a light vector that undergoes a clockwise circular motion, while left circularly polarised light describes an anticlockwise circle.

When light enters a birefringent material, such as quartz or calcite, the process is modelled in terms of the light being broken up into the fast (\\-ray) and slow (⊥-ray) components. Because the two components travel at different velocities, the waves get out of phase. When the rays are recombined as they exit the birefringent material, the polarisation state has changed because of this phase difference [45].

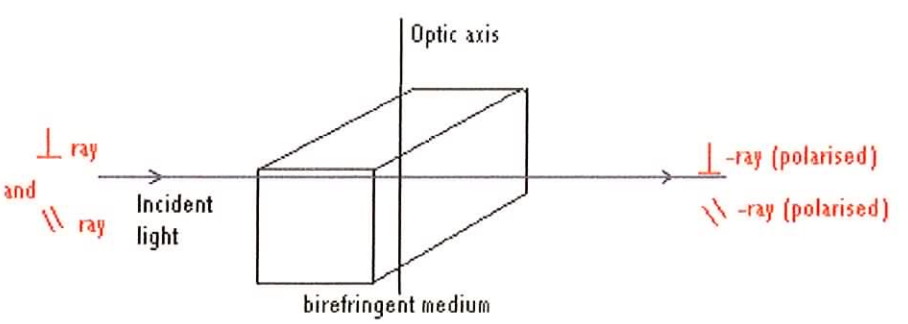

Fig.7.2. Light travelling through a birefringent medium.

Consider the propagation of plane-polarised light incident normal to a parallel-sided birefringent material, as shown in figure 7.2.

The phase difference [46] between the ⊥ and // components is given by:

$$\delta = \frac{2\pi}{\lambda}(n_e - n_o)d \qquad \text{rad.}$$

where: δ: the phase difference.

d: thickness of the birefringent material.

n_e, n_o: refractive indices of extra-ordinary and ordinary waves respectively.

λ: Wavelength

The birefringence is defined as $\Delta n=(n_e - n_o)$. The sign of this quantity can be used to indicate if the birefringent material is positive or a negative uniaxial material.

7.2. Quarter-wave plates

In this study, the wave plates we used for polarisation analysis are:

- Quartz quarter-wave plate, and
- Quarter-wave plate of Polyvinyl-alcohol film (PVA).

The specifications of these quarter-wave plates are described individually in section 7.5. One of the applications of optical thin-films is the production of quarter-wave plates. A quarter-wave plate by definition produces between the two principal planes of polarisation a phase shift of 90°, which corresponds to an optical path difference of a quarter of a wavelength. It can also produce a circularly polarised beam from a linearly polarised beam and vice versa, where the linearly polarised beam is at 45° angle to the fast and slow axes of the wave plate. Below is a schematic diagram showing production of different polarisation states using quarter-wave plates.

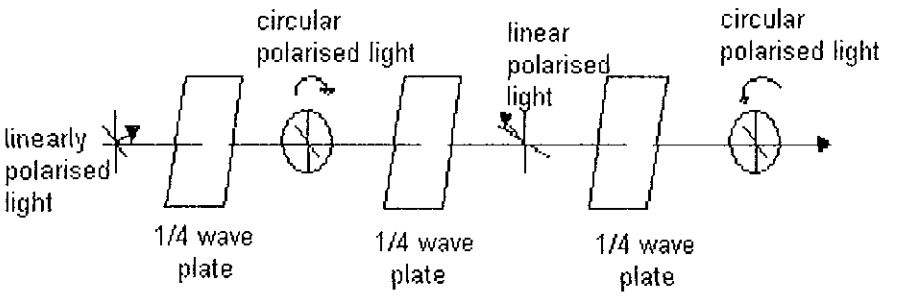

Fig.7.3. Changes of polarisation through a series of quarter-wave plates.

7.3. Phase shift analysis of a multilayer structure

In chapter 2, a description of how to grow thin film on a glass substrate, using the vacuum evaporation technique was described. Below in figure 7.4, is a schematic diagram of the grown mirror, which is a stack of alternate high- and low-index films, all one-quarter-wavelength thick [11,44,47].

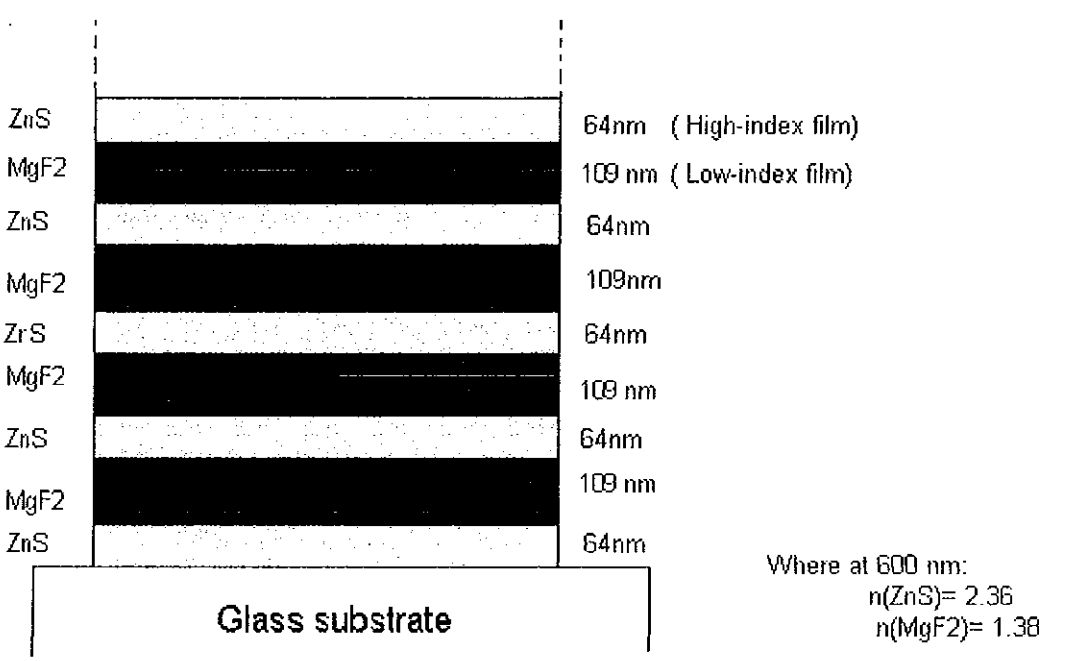

Fig.7.4. A stack of alternate high and low index films, all one-quarter wavelength thick.

To investigate the propagation of light in multilayer structure and to show how the phase shift varies at successive boundaries throughout the assembly, consider the following diagram, figure 7.5. This is important to eventually find out the total phase shift on transmission or on reflection of a multilayer structure.

Initially, light that is reflected within the high-index layers will not suffer any phase shift on reflection while those beams reflected within the low-index layers will suffer a change of π [20]. When light strikes the first surface of the structure some of it is reflected with a phase shift of π and the rest is refracted and passes through the ZnS layer with the initial phase of the incident light $+\delta$, because there is no phase change on transmission.

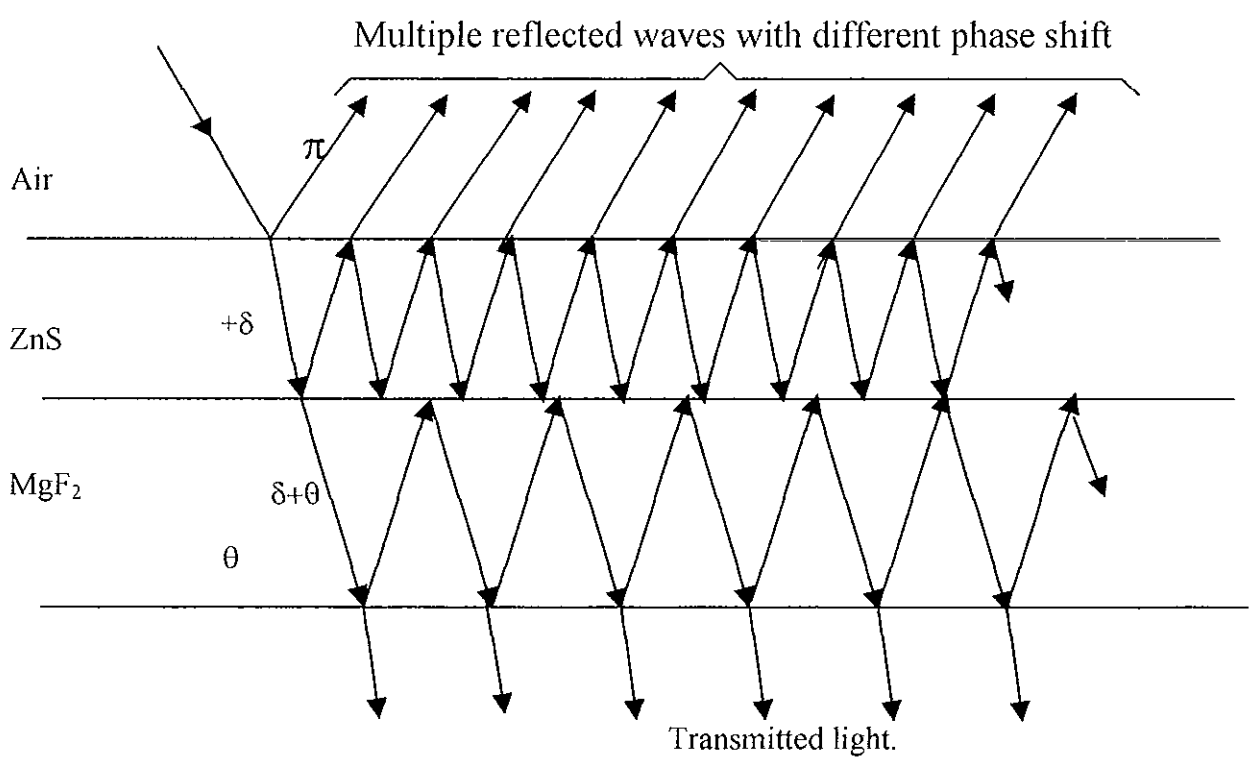

Fig. 7.5. Variable changes in phase shift associated with multiple reflections make theoretical calculations more complicated, where $+\delta$ is the initial phase of the incident light and θ is the phase shift of the beam coming with a phase of $+\delta$.

The beam itself with a phase of $+\delta$ will undergo reflection and refraction at the second boundary with a different phase shift and so on. These multiple reflections from each boundary will reappear at the front surface all in phase so that they will recombine constructively [28].

By definition, the phase angle of a complex number $Z = a + ib$ is simply:

$$\varphi = \tan^{-1}(b/a) \qquad (7.1)$$

Therefore, we can apply this definition to find out the phase angle on transmission through or on reflection from the whole structure from the calculated reflectivity and the transmission of any structure given in equations (1.15) and (1.16) respectively as described in chapter 2.

The general formulas for r and t can be written in the form of a complex number as shown below, where a_1, a_2, b_1 and b_2 are constant.

$$r = \frac{Y_0 m_{11} + Y_0 Y_s m_{12} - m_{21} - Y_s m_{22}}{Y_0 m_{11} + Y_0 Y_s m_{12} + m_{21} + Y_s m_{22}} = a_1 + ib_1$$

And $$t = \frac{2Y_0}{Y_0 m_{11} + Y_0 Y_s m_{12} + m_{21} + Y_s m_{22}} = a_2 + ib_2$$

Thus we can find easily the phase angle on transmission through or on reflection from any given multilayer structure once we know the total reflectivity and transmission of the structure.

Hence the phase angle on transmission and on reflection may be written respectively as follows:

$$\varphi_t = \tan^{-1}(b_2 / a_2) \qquad (7.2)$$

$$\varphi_r = \tan^{-1}(b_1 / a_1) \qquad (7.3)$$

7.4. Modelling the phase shift of different multilayer structures

Monitoring the phase shift on transmission as a function of wavelength for a particular multilayer structure is easy to carry out using our software.

The format of this program is laid out as shown in Appendix D, (Programme 3).

An example of phase angle calculations of a 15-layer structure is shown below in figure 7.6.

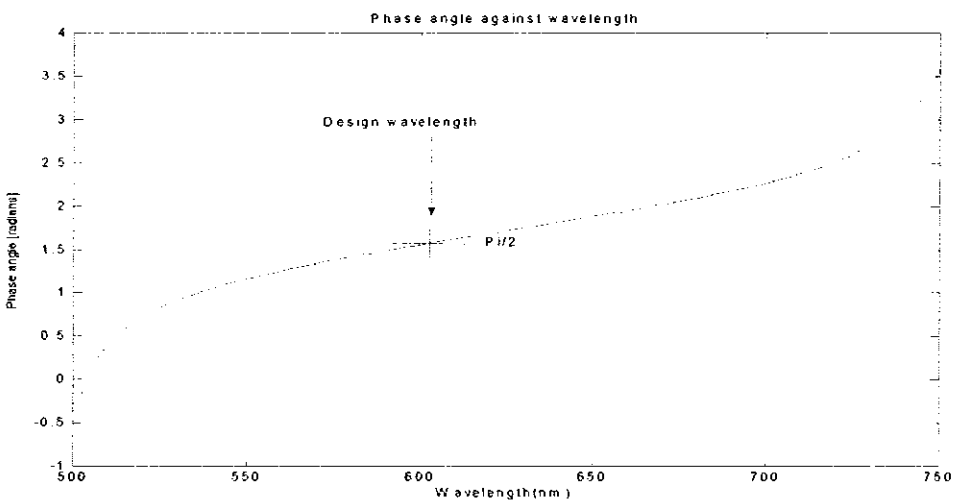

Fig.7.6. Calculated phase angle on transmission of a 15-layered thin film of alternate layers of ZnS and MgF_2 against wavelength.

The multilayer used to investigate the variations of the phase shift against wavelength consists of an odd number of layers with high-index layers on the outside, for an efficient reflection and refraction. Figure 7.6 shows that the phase shift at the central wavelength (that for which all the layers are quarter waves) is $\pi / 2$ as expected.

7.5. Phase shift analysis of birefringent plates.

Two different birefringent plates have been used in this project for phase shift analysis.

- A quartz quarter-wave plate,
- Quarter-wave plate of polyvinyl-alcohol film, PVA.

The specifications of each one are listed below [40,48].

7.5.1. Specifications of the quartz quarter-wave plate [48]

Material: Crystalline quartz.

Transmission range: 0.4 to 3 micron.

Reflection loss: 8.8% at 0.6 microns (2 surfaces).

Melting point: 1467°C

Class/Structure: Trigonal (hex)

Thickness: 2.32 mm.

Wavelength: 590 nm, (at which the plate is $\lambda/4$)

Refractive index: Table below.

Wavelength (nm)	n_o	n_e
400	1.557	1.567
442	1.553	1.562
458	1.551	1.561
488	1.549	1.558
515	1.547	1.557
532	1.546	1.556
590	1.544	1.553
633	1.542	1.551
670	1.541	1.550
694	1.540	1.549
755	1.539	1.548

Table. 2. Refractive indices of the e and o-waves of quartz against wavelength.

7.5.2. Specifications of the quarter-wave plate of Polyvinyl-alcohol film [48]

Material:	CAB (Cellulose Acetate Butyrate) supported polyvinyl-alcohol film.
Transmission:	92% (4%reflection each surface)
Colour:	clear
Thickness:	0.29 mm.
Wavelength:	640 nm, (at which the plate is $\lambda/4$)
Phase uniformity:	>8% over entire film.
Refractive index:	1.52 at 600 nm

7.5.3. Phase angle of zero-order or a multiple-order retardation plate.

(i) Zero order plates

Retardation plates and especially quarter-wave retarders are generally made of a single piece of material [49]. Zero-order waveplates are designed for those applications where a thickness is required which corresponds to a zero order phase difference. This is achieved by constructing the waveplate from two halves with their fast axes crossed. The thicknesses of these two halves are chosen so that the difference in retardation between them is equivalent to the zero order required. This kind of plate is very useful because the phase difference analysis of structure will be easy to investigate over a very short interval of wavelength. The major disadvantage of using zero or single order plates is their sensitivity to temperature and wavelength. That's why multiple order plates are commonly used for these kinds of applications.

(ii) Multiple order plates

Multiple-order retardation plates are often used to produce circularly polarised light at a single wavelength or at a discrete series of wavelengths. The plate thickness is generally of the order of one or more millimetres so that the retardation is an integral number of wavelengths plus $\lambda/4$. This plate acts like a single $\lambda/4$ plate providing it is used only at certain specific wavelengths; at other wavelengths it may not even approximate the desired retardation.

To illustrate the effect of incorporating a zero-multiple order wave plate for phase shift calculations in a multilayer structure, programme 5 (Appendix D) was created, as an example for this study. The wave plate thicknesses are chosen so that they will create a phase difference of $(2n+1)\pi/2$, where n is an integer verifying the following conditions:

- $n=0$, the wave plate is a zero order plate.
- $n\neq0$, the wave plate is a multiple order plate.

As an example, the calculated thicknesses which will create a phase difference of $\pi/2$, $3\pi/2$ and $11\pi/2$ for instance are 97.4 nm, 292.2 nm and 779.2 nm respectively, where the refractive indices of the e-wave and the o-wave are respectively: $n_e=1.553$ and $n_o=1.543$, at the wavelength 600 nm. Three multilayer cavity structures with different thicknesses of the quartz quarter wave plate are analysed for phase angle analysis. A description of a three multilayer cavity with a birefringent plate is given in the next section and the modelled results from a general multilayer structure are shown in figures 7.7 and 7.8.

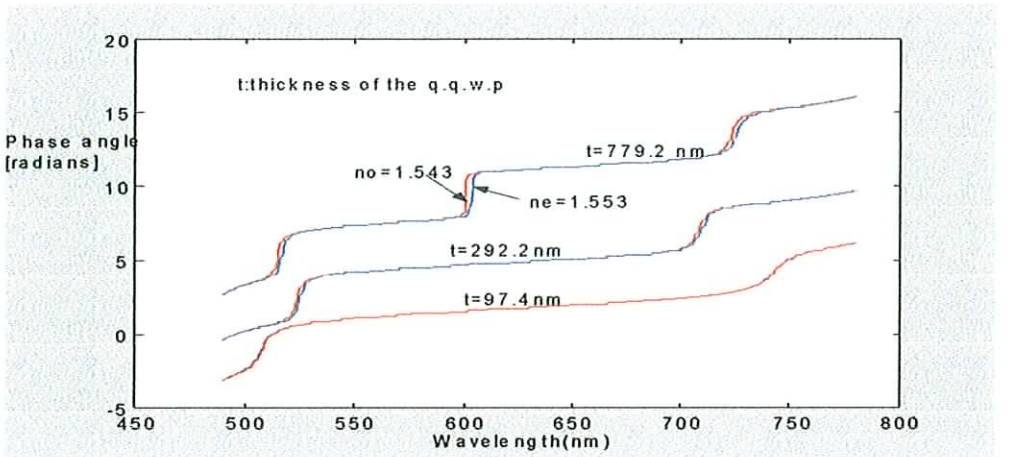

Fig.7.7. Variations of the phase angle of the ⊥ (blue curve) and \\ (red curve) components of a multilayer cavity structure with different thicknesses of quartz quarter-wave plates against wavelength.

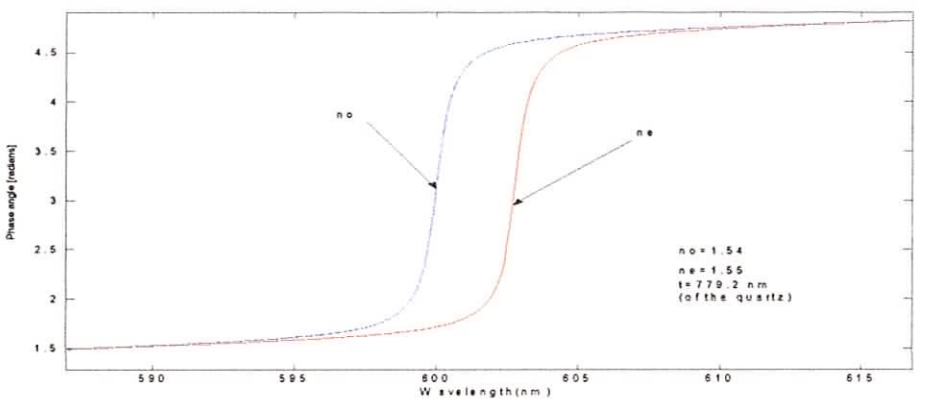

Fig.7.8. Variation of the phase angle of the ⊥ (blue curve) and \\ (red curve) components of a multilayer cavity structure with a quartz quarter-wave plate of thickness (11π /2= 779.2 nm) against wavelength.

Figure 7.8 shows the phase angle of the ⊥ and \\ components of a multilayer cavity structure with different quartz quarter-wave plates thicknesses. By increasing the thickness of the quartz quarter-wave plate (using multiple order wave plates), the phase angle spectra of the ⊥ and \\ components will increase in a stepwise behaviour. Moreover multiple order wave plates are strongly dependent on temperature, wavelength and angle of incidence [49].

7.6. Description of a multilayer cavity with a birefringent plate

In this project, we investigate the optical properties of a Fabry-Perot microcavity with a birefringent material (quartz or PVA film quarter-wave plates) by measuring the total phase shift introduced by the whole structure.

The birefringent material was sandwiched between two mirrors, which were grown by vacuum evaporation technique. The geometry of the structure to be studied is shown below, figure 7.9.

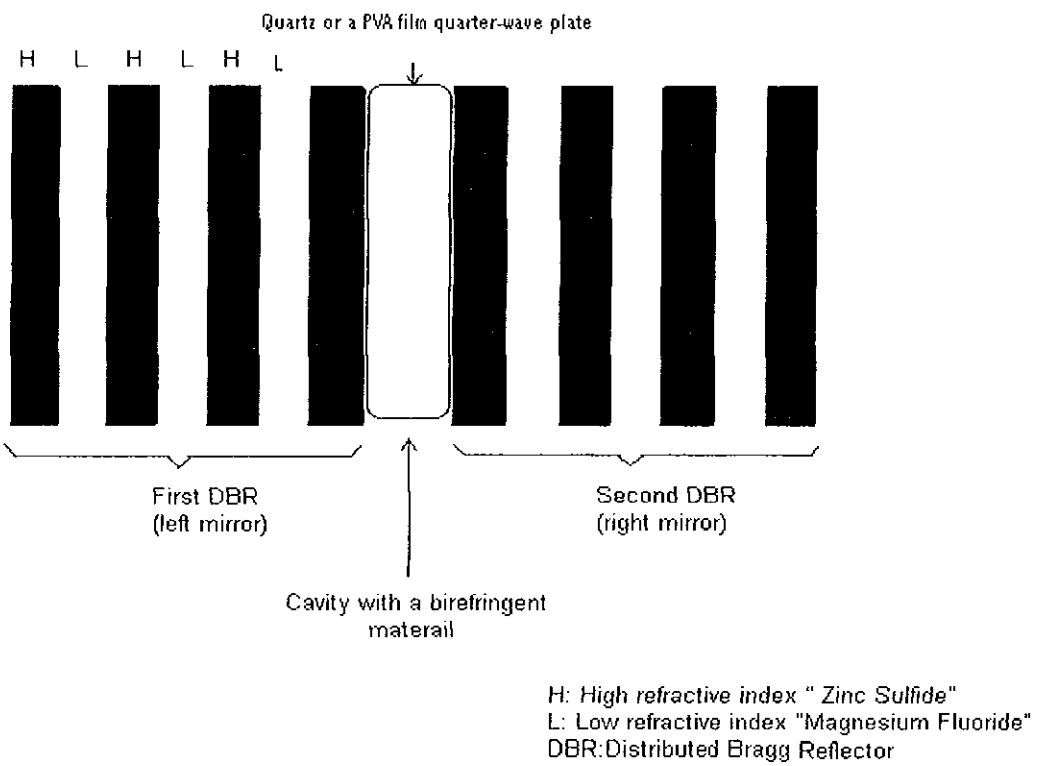

Fig.7.9. A multilayer cavity structure with quartz or a PVA film quarter-wave plate inside the cavity.

8. Experimental set-ups for polarisation measurements.

8.1. Transmission set-up.

Initial measurements made use of a transmission set-up, as shown in figure 8.1, of a He-Ne laser beam going through the Fabry-Perot cavity structure for polarisation analysis. In this section identifying the polarisation state (whether it is elliptical, circular or linear) of the light source after transmission was carried out as described below.

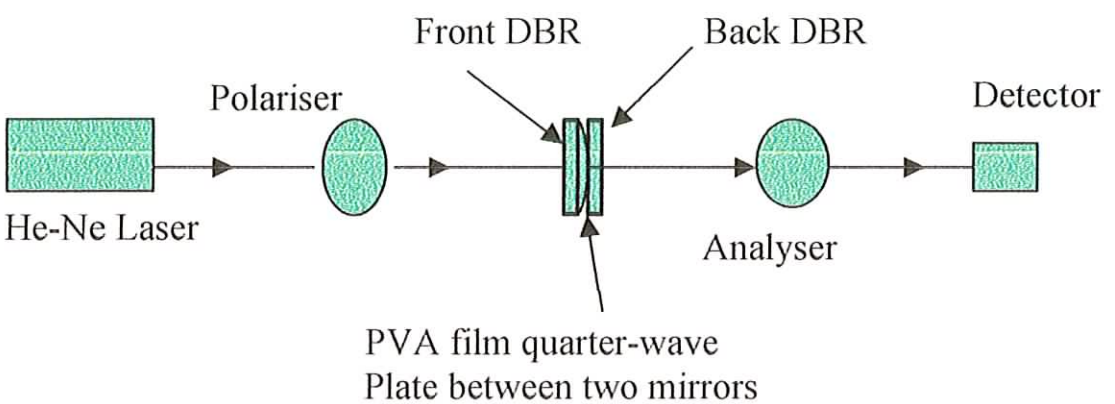

Fig.8.1. Schematic diagram of the transmission set up to investigate the polarisation state of the He-Ne laser going through a quartz quarter-wave plate sandwiched between two grown eleven-layer quarter-wave stacks of ZnS and MgF_2 Mirrors.

8.2. Procedure

Before taking the readings, the orientations of the polarisers and wave plates must be adjusted:

- First of all make sure the two polarisers are parallel. That way, it is fine to work with an offset from 0^0. To do this, keep the first polariser fixed, and rotate the second polariser until you observe a minimum in transmission. At this point the polarisers

are oriented 90° apart. Rotate the second polariser 90° so that the polarisers are now parallel.

- Mount the Polyvinyl-alcohol quarter-wave film on a rotation stage and position it between the polarisers.
- Rotate the PVA wave plate so that its fast axis is making a 45° angle with the vertical.

The results of the first experiment (PVA quarter-wave plate only), and of the second (real structure), are tabulated in table 3.

Angle of analyser in °	Intensity of the transmitted light (Only the PVA film) I / mW	Intensity of the transmitted light (Real structure) I / μW
0	0.209	3.94
10	0.220	3.92
20	0.237	3.98
30	0.257	4.10
40	0.277	4.29
50	0.295	4.52
60	0.308	4.76
70	0.313	4.97
80	0.313	5.14
90	0.306	5.26
100	0.294	5.36
110	0.280	5.38
120	0.262	5.28
130	0.242	5.13
140	0.226	4.93
150	0.211	4.70
160	0.205	4.51
170	0.205	4.31
180	0.212	4.14

Table. 3. Results of polarisation on transmission for the PVA film only and for the cavity structure.

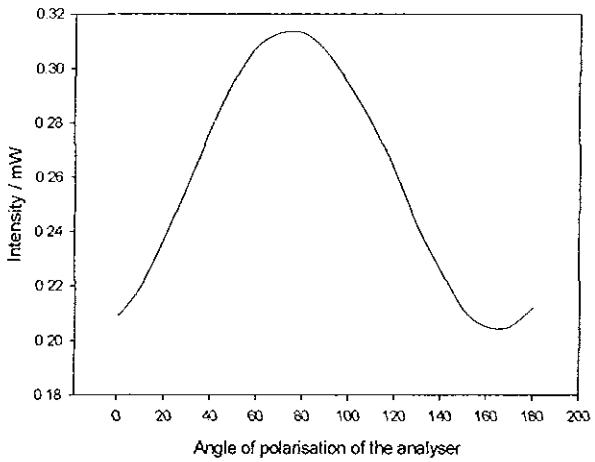

Fig. 8.2. Intensity of the transmitted light going through a PVA film against the angle of polarisation of the analyser.

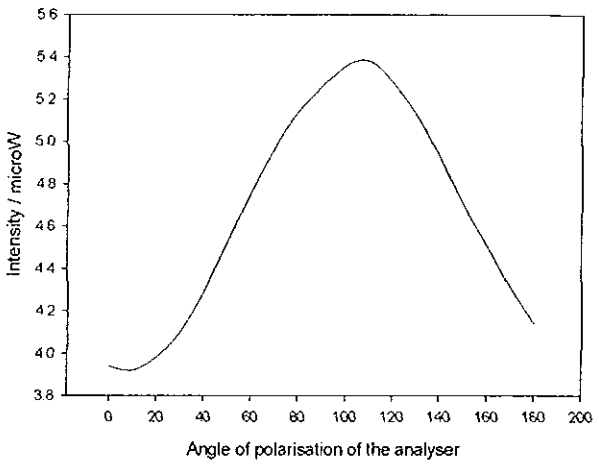

Fig.8.3. Intensity of the transmitted light going through DBR/PVA/DBR against the angle of polarisation of the analyser.

Figures 8.2 and 8.3 show that the polarisation state of light was changed once the PVA was sandwiched between two DBRs. The shift between the peaks of the two spectra was found to be 40 degrees, which is due mainly to the existence of the PVA (birefringent material) inside the cavity. Although it is a spectral shift we still get elliptically polarised light instead of circularly polarised light (constant intensity), the expected result.

These results are useful in trying to predict the state of polarised light, but are not going to satisfy our aim, since modelling the structure (as will be covered later on) indicates that the transmission spectra of the $\perp$ and \\ components can only be distinguished over a very small range of wavelengths. This is because the thickness of the quartz/PVA quarter-wave plates is so large compared to the total thickness of the multilayer stack. Because of temperature and thickness sensitivity, single wavelength measurements are inconclusive. It is necessary to examine the structure over a range of wavelengths. The use of the Perkin-Elmer UV-vis / IR spectrometer was implemented for this kind of measurement.

8. 3. Birefringent materials and phase shift analysis.

8. 3. 1. Phase shift of the quartz quarter-wave plate and PVA.

(i) Quartz quarter-wave plate

In order to see the variation of the phase difference of the quartz quarter-wave plate against wavelength, programme 5 (Appendix D) was created as an example for this kind of calculation.

The quartz plate is designed for 590 nm. This result confirmed from our modelling (as shown in figure 8.4 (b)) that the phase shift at 590 nm is $\pi/2$.

Figure 8.4 (a) shows the sensitivity of the quartz plate against wavelength. This is due to the large thickness of the plate.

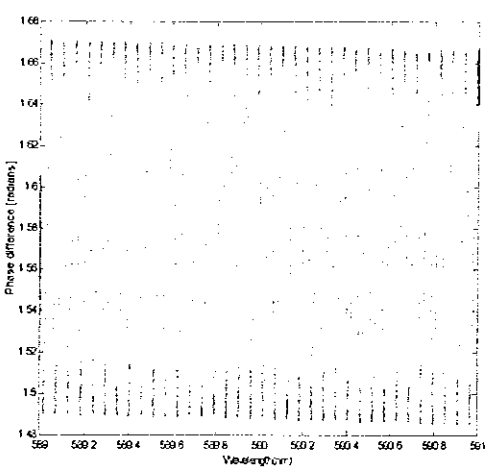

Fig.8.4.(a). Variations of the calculated phase difference of the quartz quarter wave plate against wavelength. (long interval)

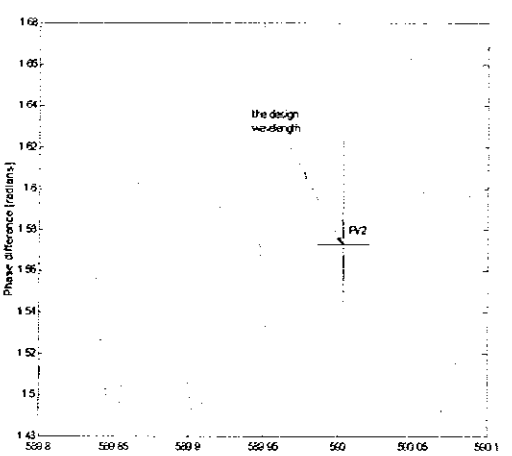

Fig. 8.4 (b). Variations of the calculated phase difference of the quartz quarter wave plate against wavelength (around the design wavelength)

(ii) PVA quarter-wave plate film.

A similar calculation was carried out for the PVA quarter-wave plate. Figures 8.5 (a) and 8.5 (b) show that the phase difference at $\lambda = 640$ nm for which the plate is a quarter wave plate is $\pi / 2$, the expected value.

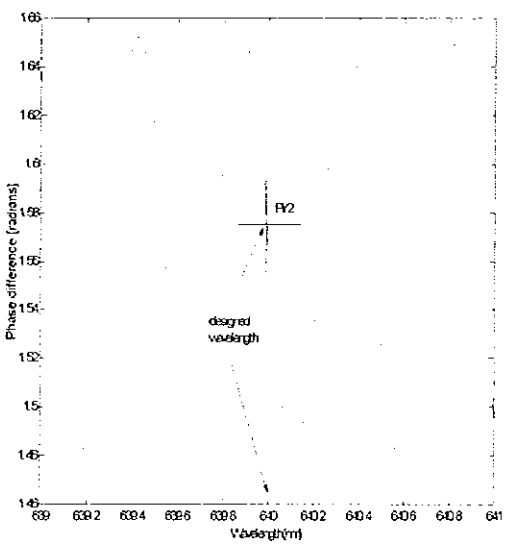

Fig. 8.5. (a). Calculated phase difference of the PVA quarter wave plate against wavelength. (around the design wavelength).

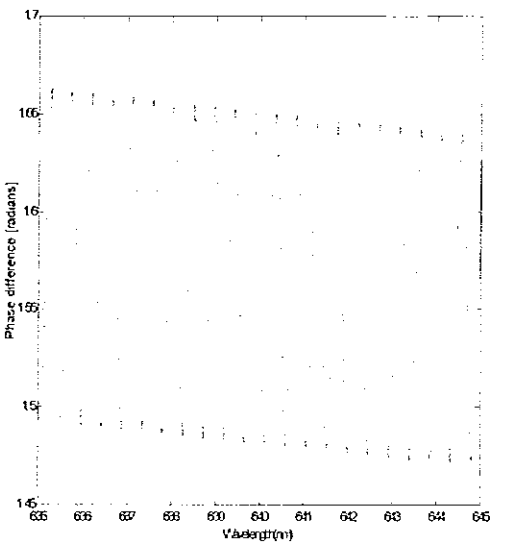

Fig. 8.5 (b). Calculated phase difference of the PVA quarter wave plate against Wavelength, (long interval)

8.4. Phase shift analysis of the multilayer cavity with PVA

8.4.1. Total phase difference between the ⊥ and the \\ components.

Figures 8.6 (a) and 8.6 (b) show the calculated total phase difference for the PVA quarter wave plate sandwiched between two grown films, against wavelength. Each mirror was made of 11 alternating layers of ZnS and MgF_2.

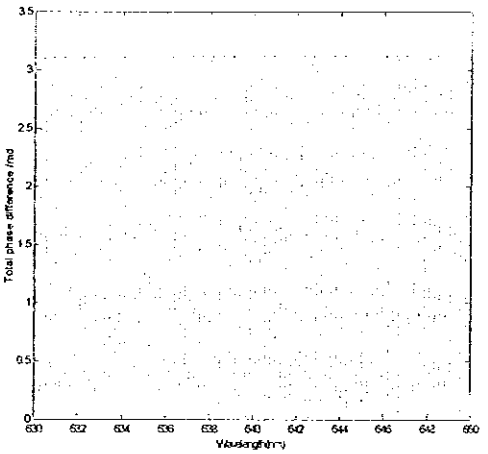

Fig.8.6 (a). Calculated total phase difference of the PVA quarter wave plate sandwiched between two grown films, against wavelength. (long interval)

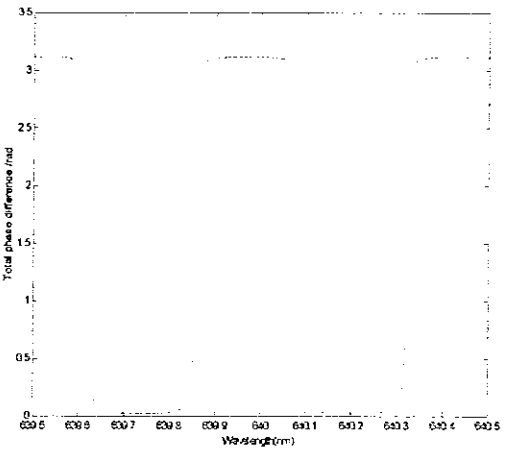

Fig.8.6 (b). Calculated total phase difference of the PVA quarter wave plate Sandwiched between two grown films against wavelength, (around 640 nm).

8.4.2. Effect of the Birefringence on transmission

In order to illustrate the effect of the birefringence on transmission, two different values of Δn for the same structure were used:

$\Delta n1 = n_e - n_o = 1.52055 - 1.52 = 0.005$ (red curve)

$\Delta n2 = 0.03$ (blue) where n_o is fixed.

Figure 8.7 shows that the spectral shift between the $\perp$ and \\ components L1 (shown on figure 8.7 associated with bigger birefringence, $\Delta n2$) is greater than L2 (for small birefringence, $\Delta n1$).

Therefore for an ideal birefringent material to be inserted into the cavity for polarisation analysis, we need:

- Thinner thickness of the plate so that its performance won't be sensitive to different parameters such as temperature and wavelength.

- Bigger birefringence for bigger phase shift. This factor will enable us to distinguish spectrally between the ⊥ and \\ components.

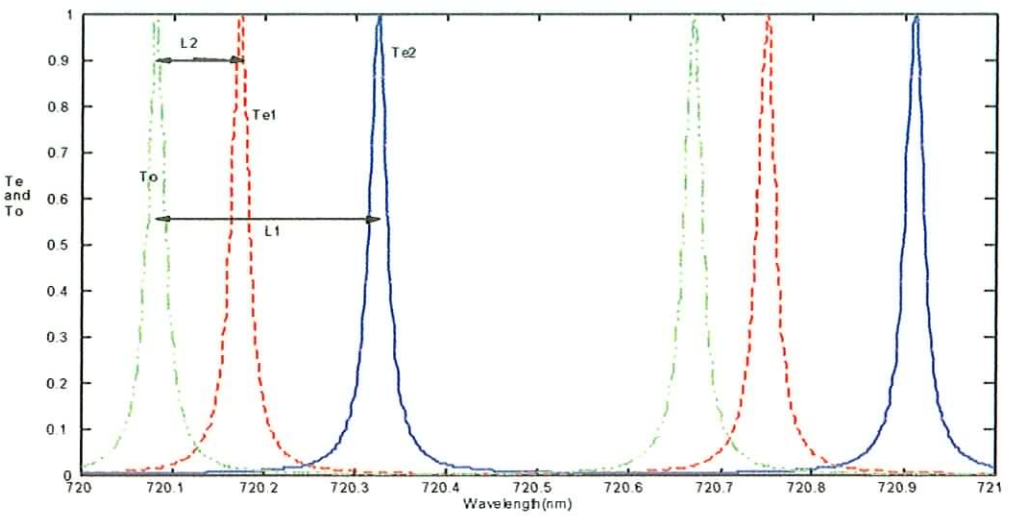

Fig.8.7. Modelling the transmission of the ⊥ component (green graph) and \\ components (red and blue) of the whole structure for different birefringence, where L1 and L2 are the spectral shift between the ⊥ and \\ components for two different birefringence, and To and Te represent the ⊥ and \\ respectively.

8. 5. Polarisation measurements of the microcavity structure

Transmission spectra of the multilayer cavity structure for different polarisation states are measured within a very small range of wavelengths (2 nm) using a Pekin-Elmer spectrometer. The microcavity structure consisted of two grown mirrors of eleven alternating layers of ZnS and MgF_2. The cavity was created by sandwiching the quarter-wave plate of polyvinyl alcohol film (PVA) with the two grown mirrors. Two binder clips were used to hold tight the two mirrors parallel. This is important in order to be able to see the Fabry-Perot fringes. Even though we tried to position the two mirrors parallel to create the cavity, it is still slightly wedged, thus we expect

some experimental errors in our results. The procedure can be summarised as described below.

8.5.1. Procedure

In general, the procedure in getting these transmission spectra involved understanding the optics of the Perkin-Elmer UV-vis spectrometer. This is of course will require supplying the instrument with a polariser, and setting up the instrument parameters which will suit our measurements for getting high resolution.

These parameters are set manually from the first Control Window:

- Ordinate Mode: should be on %T
- Data Interval: use the lowest data interval of the instrument, which is 0.01nm, (working at the resolution limit which will cause a noisy graph).
- Integration Time: Higher integration time will definitely reduce noise.
- Scan Speed: Shows the scan speed in nm/min. Because we are interested in narrow bands, the use of slow scan speeds will improve the signal-to-noise ratio.
- Slit Mode: Slit width is in nm. Set a narrower slit to increase the spectral resolution of the peaks.

On the right side of the Control Window, the Instrument Page contains some tabs. Click on Optics tab, then on the following buttons:

- Common beam Mask Dialog: is used to reduce the beam height for operation with micro cells. So a % 5-10 is suitable for our measurements. This feature helped us a lot to see the spectral shift because the cavity originally was not parallel, and by

examining a smaller area of the sample, the local variation in parallelism is minimised.

- Monochromator and Detector dialogs are set outside the scanning region of our interest.
- Common Beam Depolariser: is off, once we are not using the polariser, and is on when the polariser is inserted.
- Scanning region: 798-800 nm.

Now the instrument is ready for action and everything is placed at the right place.

(i) The first thing to do is a background spectrum where two microscopic glass slides were placed in the reference arm and the sample arm.

(ii) With no polariser on, run the spectrum as usual.

(iii) With the polariser on, set it up at 0°, and run the transmission spectrum.

(iv) With the polariser on set at 90°, get the third graph.

8.5.2. Results

The measured transmission spectra of the multilayer cavity structure with PVA for different polarisation states are illustrated below in figure 8.8.

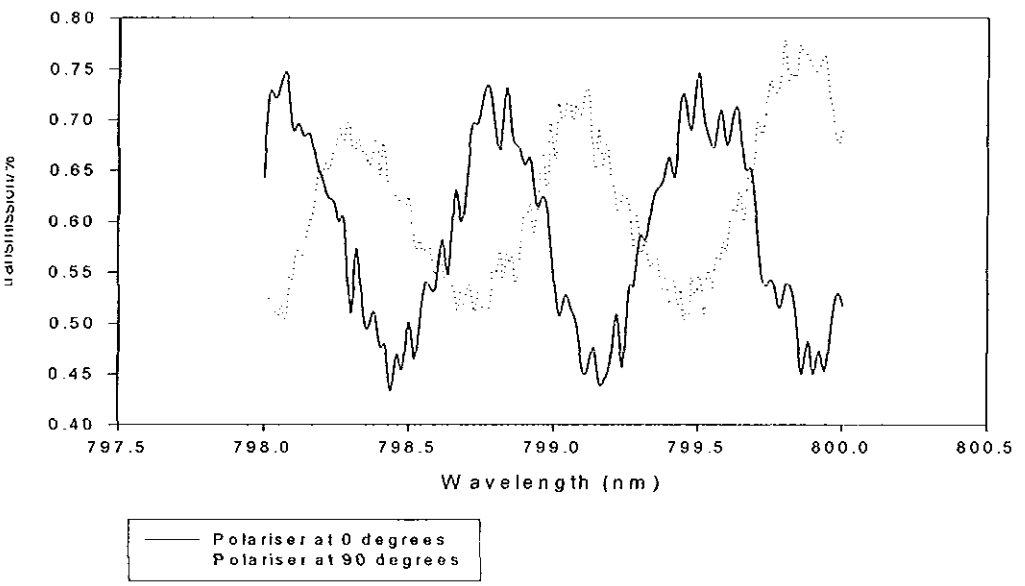

Fig.8.8. Measured Transmission spectra of the multilayer cavity with PVA for different polarisation states.

The dotted and the continuous graphs represent the measured transmission with polariser at 90 and 0 degrees respectively.

The measured spectral shift between the ⊥ and the \\ components -waves was found to be 0.2804 nm.

To compare the measured results with the theoretical results from modelling, figure 8.9 shows the results of modelling this multilayer cavity structure.

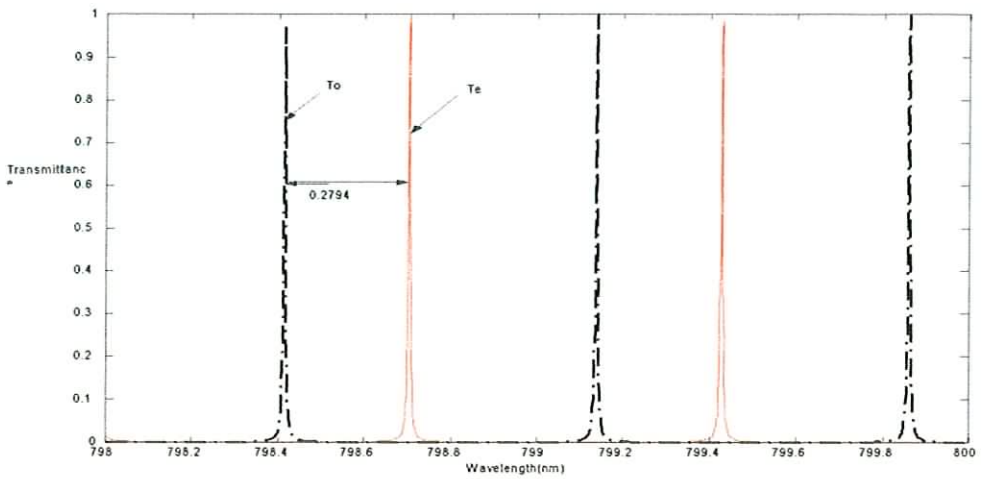

Fig.8.9. Calculated transmission spectra of the e and the o-waves of the multilayer cavity structure with PVA

The resolution of the modelled peaks in figure 8.9 is very high in comparison to the measured one obtained in figure 8.8. This is because the model can give better results than the resolution of the Perkin-Elmer spectrometer, and also because of sample imperfections (lack of parallel plates, perfect mirror etc.)

The calculated phase shift between the $\perp$ and the \\ components from the modelling spectrum is about: 0.2794 nm.

Thus, the measured spectral shift between these two different polarisation states of the multilayer cavity structure is in good agreement with the calculated results from the modelling, showing that modelling works.

9. Conclusion

The aim of the project was to investigate a simple one-dimensional photonic bandgap structure, which is known as the Fabry-Perot microcavity structure, by incorporating birefringent materials inside the cavity. This has been achieved through successful steps throughout the progress of the project, which can be laid out as follow:

(i) Commission new evaporator unit.

(ii) Making multilayer thin films structures of ZnS and MgF_2 using the vacuum evaporation technique.

(iii) Run the UV-vis spectrum of each film in order to characterise it spectroscopically.

(iv) Model the test structures using MATLAB software with and without dispersion.

(v) Phase shift analysis of any multilayer cavity structure.

Growing high reflectivity distributed Bragg reflector (DBR) to form the mirrors of the Fabry-Perot cavity was achieved successfully, where a simple DBR consists of multiple layers of alternating high-and low-index materials arranged periodically and the thickness of each layer is chosen so as to satisfy the Bragg quarter-wave condition, that is:

$$d = \frac{\lambda_0}{4n}$$

Therefore in order to predict the thickness of each grown layer of Zinc Sulfide and Magnesium Fluoride, we modelled the measured transmission of the mirror with a corresponding fitted curve. In this way we know accurately the thickness of each layer.

Finally incorporating phase shift into one model was carried out successfully, where measuring the total phase shift of a light beam going through the whole multilayer structure was fully investigated. The results show that the measured phase shift between these two different polarisation states of the multilayer cavity structure is in good agreement with the calculated results from the modelling.

We now have a good modelling tool to explore the effect of birefringent material in multilayer cavity structures.

Suggested future work to be considered for a typical research in this field can be summarised as follows:

Instead of inserting a birefringent material plate between two grown mirrors to create the cavity, spin coating of a thin polymer layer directly onto a mirror will definitely solve the problems of thickness and uniformity in order to see the spectral shift without trying to confine our investigations over a small range of wavelengths. The advantage of this technique is that the thickness and the birefringence of the material can be chosen to be small and big respectively for study. A typical example of implementing this technique in a similar study was carried out by Bradley [18]. This will open the way to studying a range of optical structures.

References

[1] Sievenpiper DF, Yablonovitch E, Winn JN, et al. "3D Metallo-Dielectric photonic crystals with strong capacitive coupling between metallic islands", Phys. Rev. Lett, Vol. 80, No. 13, 2829-2832, March (1998).

[2] Boroditsky M, Krauss TF, Coccioli R, et al. "Light extraction from optically pumped light-emitting diode by thin-slab photonic crystal", Applied Physics Letters, Vol. 75, No. 8, 1036-1038 AUG 23, (1999).

[3] E. Yablonovitch, "Photonic bandgap structures", Journal of Optical Society of America, Vol. 10, No. 2, 283-295, (1993).

[4] I. Abram, G.Bourdon, "Photonic-well microcavities for spontaneous emission control", Physical Review A, 54, 3476-3481, (1996).

[5] A. Birner, A.-P. Li, F. Muller, "Transmission of a microcavity structure in a two-dimensional photonic crystal based on macroporous silicon", Materials Science In Semiconductor Processing, Vol. 3, 487-491, (2000).

[6] Ji Zhou, Y. Zhou, S. L. Ng, H. X. Zhang, " Three-dimensional photonic band gap structure of a polymer-metal composite", Applied Physics Letters, Vol.76, No. 23, June (2000).

[7] E. Yablonovitch, Inhibited Spontaneous Emission in Solid- State Physics and Electronics, Physical review Letters, 58, 2059-2061, (1987).

[8] G. Björk, S. Machida, and K. Igata, "Modification of spontaneous emission rate in planar dielectric microcavity structures," Phys. Rev. A, 44, 669-681 (1991).

[9] E. Snoeks, A. Lagendijk, and A. Polman, "Measuring and Modifying the Spontaneous emission rate of Erbium near an Interface", Physical Review Letters, Vol. 74, No. 13, 2459- 2462 (1995).

[10] K. Tanaka, T. Nakamura, W. Takamatsu, M. Yamanishi, Y. Lee, and T. Ishihara, "Cavity- induced changes of spontaneous emission lifetime in one-dimensional semiconductor microcavities," Phys. Rev. Lett, Vol. 74, 3380-3383 (1995).

[11] L. A. Graham, D. L. Huffaker, Q. Deng, and D. G. Deppe, "Controlled spontaneous lifetime in microcavity confined InGaAlAs/GaAs quantum dots," Applied Physics Letters, Vol. 72, 1670-1672 (1998).

[12] M. D. Tocci, M. J. Bloemer, M Scalora, J. P. Dowling , "Thin-film nonlinear optical diode", Appl. Phys. Lett. Vol. 66, 2324-2326, (1995).

[13] Youngkwon Yoon, Jongin Shim, "Transmission spectra of Fabry-Perot etalon filter for diverged input beams", IEEE Photonics Technology Letters, Vol. 14, No. 9, 1315-1317, September (2002).

[14] Ludovic Escoubas, Francois Flory. "Fabry-Perot multilayers for enhancing the diffraction efficiency of ion-implanted gratings", Applied Optics, Vol. 40, No. 10, 1587-1592, (2001).

[15] A. V. Selkin, A. A. Dukin, N. A. Feoktistov, " Optical properties of a Fabry-Perot microcavity with Er-doped hydrogenated amorphous silicon active layer", Applied Physics Letters, Vol. 77, No. 19, November (2000).

[16] Q. Deng and D. G. Deppe, "Spontaneous lifetime in a dielectrically apertured Fabry-Perot microcavity", Optics Express, Vol. 2, No. 4, 157-161, (1998).

[17] Bianca E. Nelson, Martina Gerken, David A. B. Miller, " Use of a dielectric stack as a one-dimensional photonic crystal for wavelength demultiplexing by beam shifting", Optics Letters, Vol. 25, No. 20, October (2000).

[18] T. Virgili, D.G. Lidzey ,D.D.C. Bradley, " Completely polarised photoluminescence emission from a microcavity containing an aligned conjugated polymer ", Chemical Physics Letters, 341, 219-224, June (2001).

[19] T. Vigili, D.G. Lidzey, D.D.C. Bradley, " Influence of the orientation of liquid crystalline poly(9,9-dioctylfluorene) on its lasing properties in a planar microcavity", Applied Physics Letters, Vol. 80, No. 22, June (2002).

[20] Hecht Eugene, Optics book, Fourth edition, 416-431, (2001).

[21] Michael Mazilu, Alan Miller, and Vesselin T. Donchev, " Modular method for calculation of transmission and reflection in multilayerd structures ", Applied Optics, Vol. 40, No. 36, December (2001).

[22] The Math works, MATLAB book, The language of Technical Computing, Version 5, (1999).

[23] Elliot Scientific Ltd, CVI spectral products handbook, pp16-18, 36-37, (2000).

[24] Azzam RMA, Mahmoud FA, " Symmetrically coated pellicle beam splitters for dual quarter-wave retardation in reflection and transmission ", Applied Optics, Vol. 41. No. 1, 235-238, January (2002).

[25] Huang DW, Yang CC, " Reconstruction of fiber grating refractive-index profiles from complex Bragg reflection spectra ", Applied Optics, vol. 38, No. 21, 4494-4499, July (1999).

[26] Cleary D.D, Nichols JW, Davis DC, "Design for an all-reflection Michelson interferometer ", Applied Optics, Vol. 34, No. 4, 433-435, February (1992).

[27] Holland L, " Vacuum deposition of thin films ", pp. 3 – 120, (1956).

[28] Macleod H. A, " thin-film optical filters ", pp. 4 – 7, 200 – 245, (1969).

[29] Donald L. Smith, "Thin-film deposition, principles & practice", (1995).

[30] Ramaiah KS, Su YK, Chang SJ, et al, " Characterisation of Cu doped CdSe thin films grown by Vacuum evaporation ", journal of Crystal Growth, 224 (1-2), 74-82, April (2001).

[31] Shivalingapp L, Srinivasan Mp, Mohan S, " Highly stable oscillator for quartz crystal thickness monitor, Vacuum, Vol. 42, No. 3, 203-204, (1991).

[32] El Zawawi IK, Abdel-Moez A, Terra FS, et al, " Substrate temperature effect on the optical and electrical properties of antimony trisulfide thin films ", Thin Solid Films, 324 (1-2), 300-304, July (1998).

[33] Katumba G, Olumekor L, " Effects of thickness and composition on the resistivity of $CuMgF_2$ cermet thin film resistors ", Journal of Material Science, Vol. 35, No. 10, 2557-2559, May (2000),

[34] Lauran, 'The Photonics Handbook' (1991).

[35] DECTAK manual, Version 5.

[36] Perkin-Elmer UV-vis spectrometer manual.

[37] John Doran, Mcontrol MATLAB program for calculation of the optical properties of multilayered structures, 1998.

[38] Peiris FC, Bindley U, Furdyna JK, et al, " Determination of the dispersion of the index of refraction and the elastic moduli molecular-beam-epitaxy-grown Znl-xBexSe alloys ", Applied Physics Letters, Vol. 79, No. 4, 473-475 July (2001).

[39] BI WG, LI AZ, " the dispersion of the refractive index of III-V Semiconductors ", Journal of Applied Physics, Vol. 71, No. 6, 2826-2829, March (1992).

[40] http://www.crystran.co.uk

[41] http://www.umadvancedmaterials.com/iroptics

[42] Mark J. Bloemer and Michael Scalora, "Transmissive properties of Ag/MgF_2 photonic band gaps ", Applied Physics Letters, Vol. 72, No. 14, 1676-1678, April (1998).

[43] Schwarzl T, Springholz G, Seyringer H, et al, " High-reflectivity lead-salt-based Bragg mirrors for the mid infrared range ", IEEE Journal of quantum Electronics Vol. 35, No. 12, 1753-1758, December (1999).

[44] Escoubas L. Flory F, Lemarchand F., and During A, " Enhanced diffraction efficiency of gratings in multilayers ", Optics Letters, Vol. 25, No. 4, 194-196, February (2000)

[45] F. Graham Smith and A. King, Textbook of " Optics and photonics An Introduction ", Chapter 6, (2000).

[46] Kazimierz Pietraszkiewicz, Wladyslaw A. et al, " Effect of multiple reflections in retardation plates with elliptical birefringence ", Journal Of Optical Society of America A, Vol. 12, No. 2, 420-424, February (1995).

[47] Michael F. Weber, Carl A. Stover, Larry R et al, " Giant Birefringent Optics in Multilayer Polymer Mirrors ", Science Magazine, Vol. 287, 2451-2456, March (2000).

[48] Edmund Scientific Catalogue, page 74, (2002).

[49] J. M. Bennett, "Handbook of optics", Vol. II, Chapter 3.

[50] J. C. Wyant, C. L. Koliopoulos, B. Bhushan, et al, " Development of a three-dimensional noncontact digital optical profiler ", Journal of Tribology. Vol. 108, 1-8, January (1986)

[51] J. C. Wyant, C. L. Koliopoulos, B. Bhushan, et al, " An optical profilometer for Surface Characterisation of magnetic media ", ASLE Transactions, Vol. 27, 101-113, April (1984)

[52] J. C. Wyant, C. L. Koliopoulos, B. Bhushan, " Measurement of surface topography of magnetic tapes by Mirau interferometer ", Applied Optics, Vol. 24, No. 10, 1489-1497, May (1985).

List of figures

Appendix A

----------List of variables that were used to write MATLAB programs----------

n	refractive index vector
n_0	refractive index of incident material
n_s	refractive index of exit material
a	angle of incidence.
a_4	exit angle.
m = 1: 3	m=1, m=2 and m=3
a_m	angle vector
d	thickness vector
M_m	the characteristic matrix vector
L	wavelength
L= 300: 5: 700	wavelength vector increasing by step of 5
r	coefficient of reflection
t	coefficient of transmission
R	Reflectance vector
T	Transmittance vector
RR (cc)	Reflectance calculation
TT (cc)	Transmittance calculation
LL (cc)	specific wavelength in wavelength calculation

<Program 1>

```
---------------Nine-layered thin film-------------

n0=1; % the refractive index of air.
ns=1.5; % the refractive index of substrate.
a = 0; % the angle of incidence.
A = sqrt(8.854* 10^-12 ./(4*pi*10^-7)); % constant
% refractive index vector of ZnS and MgF2, where n(ZnS)=2,34
and n(MgF2)=1.38.
n =[1.38 2.34 1.38 2.34 1.38 2.34 1.38 2.34 1.38];
% layer's thickness vector of ZnS and MgF2 , where d(ZnS)=64
and d(MgF2)=108 nm.
d = [108 64 108 64 108 64 108 64 108]; % in (nm)

% The equations below for reflectance and transmittance
calculations are extracted from chapter 1.
% The use of "for loop" will allow us to repeat a group of
statements for predetermined number of times.
cc=0;
for L=300:5:1200 % wavelength interval with an increment of 5
    M =1;
   cc=cc+1;
     for m = 1:9
        am = asin(n0*sin(a) ./n(m));
        a4 = asin(n0*sin(a) ./ns);
        hm = n(m)*d(m)*cos(am);
        ym = A*n(m)*cos(am);
        y0 = A*n0* cos(a);
        ys = A*ns* cos(a4);
        k = 2*pi ./L;

       Mm = [cos(k*hm) i*sin(k*hm)./ym; ym*i*sin(k*hm)
            cos(k*hm)];
        M = Mm*M;

    end
   % Reflectivity
  r = (y0*M(1,1) + y0*ys*M(1,2) - M(2,1) - ys*M(2,2))
      ./(y0*M(1,1) +   y0*ys*M(1,2) + M(2,1) + ys*M(2,2));

  % Transmitivity
  t = 2*y0 ./(y0*M(1,1) + y0*ys*M(1,2) + M(2,1) +
      ys*M(2,2));

  R = r*conj(r);% Total reflectance
```

```
  T = t*conj(t);% Total transmittance
  RR(cc)=R; TT(cc) =T; LL(cc)=L;
End % end of the loop.
% Now you can plot graphs
figure
plot(LL,RR);
title('reflectance against wavelength');
xlabel('wavelength(nm)');
ylabel('reflectance');
```

<Program 2>

```
-------------Fifteen-layered thin film-------------

n0= 1; % the refractive index of air.
ns= 1.54; % the refractive index of substrate.
a = 0;% the angle of incidence

A = sqrt(8.854* 10^-12 ./(4*pi*10^-7)); % constant
% layer's thickness vector of ZnS and MgF2 , where d(ZnS)=64
% and d(MgF2)=108 nm.

d = [108 64 108 64 108 64 108 64 108 64 108 64 108 64   108];
% refractive index vector of ZnS and MgF2, where n(ZnS)=2,34
% and n(MgF2)=1.38.

n = [1.38 2.34 1.38 2.34 1.38 2.34 1.38 2.34 1.38 2.34
     1.38 2.34 1.38 2.34 1.38];

% Same as program 1, all
cc=0;
for L=300:5:1200 % wavelength interval with an increment of 5
    M=1;
    cc=cc+1;
    for m = 1:15
        am = asin(n0*sin(a) ./n(m));
        a10 = asin(n0*sin(a) ./ns);
        k  = 2*pi ./L;
        hm = n(m)*d(m)*cos(am);
        ym = A*n(m)*cos(am);
        y0 = A*n0* cos(a);
        ys = A*ns* cos(a10);
        Mm = [cos(k*hm) i*sin(k*hm)./ym; ym*i*sin(k*hm)
              cos(k*hm)];

        M = Mm*M;
    end
```

```
        r=(y0*M(1,1) + y0*ys*M(1,2) - M(2,1) -  ys*M(2,2))
             ./(y0*M(1,1) + y0*ys*M(1,2) + M(2,1) + ys*M(2,2));
        t = 2*y0 ./(y0*M(1,1) + y0*ys*M(1,2) + M(2,1) +
             ys*M(2,2));
         R = r*conj(r);
         T = t*conj(t);
        RR(cc)=R;
        LL(cc)=L;
        TT(cc) =T;
end
figure
plot(LL,RR)
Title('Reflectance against wavelength');
xlabel('Wavelength(nm)');
ylabel ('Reflectance ');
```

Appendix B

(B1) Control Window.

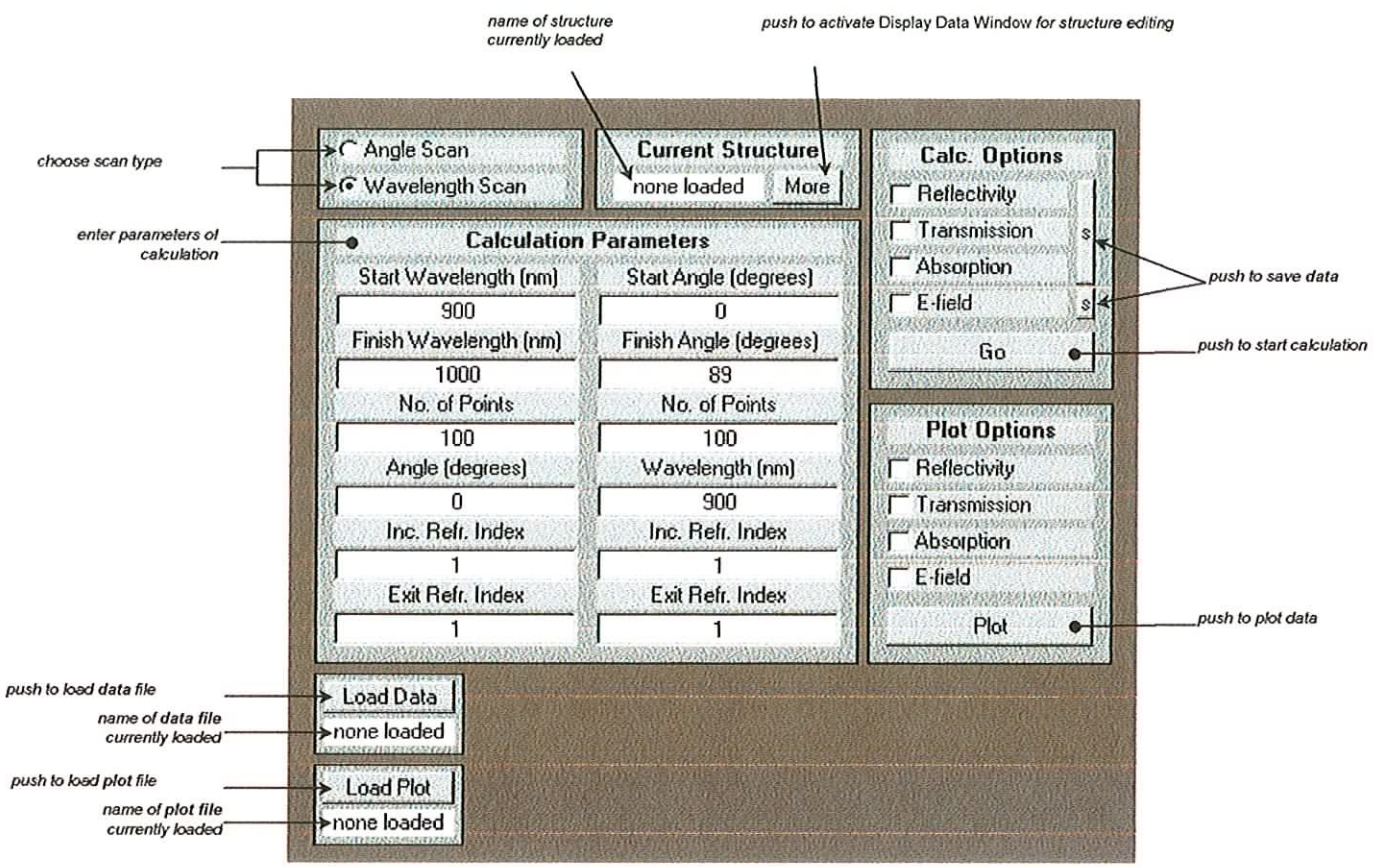

(B2) Display Data Window.

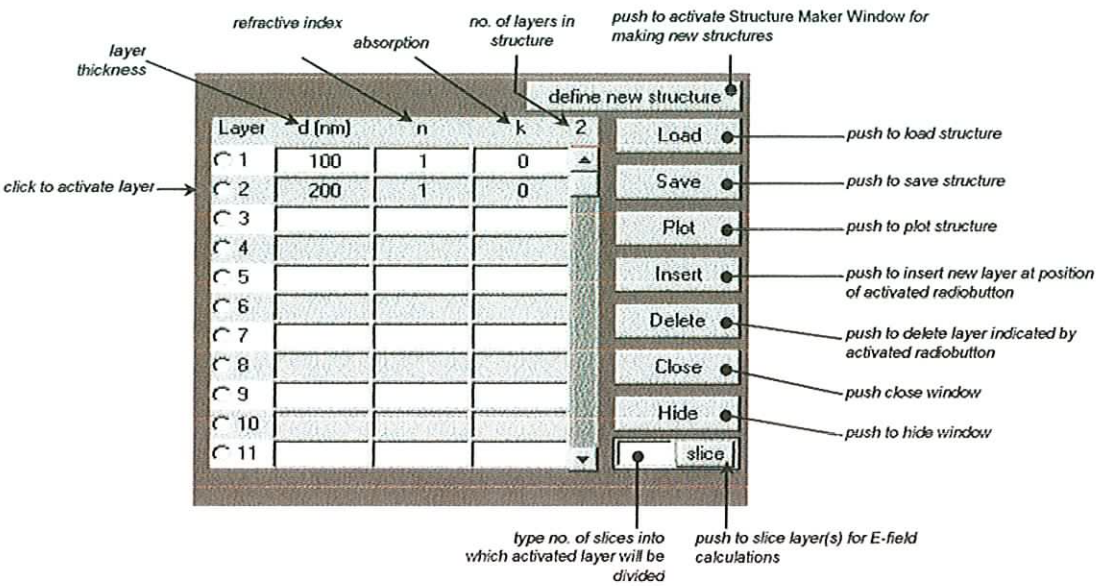

(B3) Structure Maker Window.

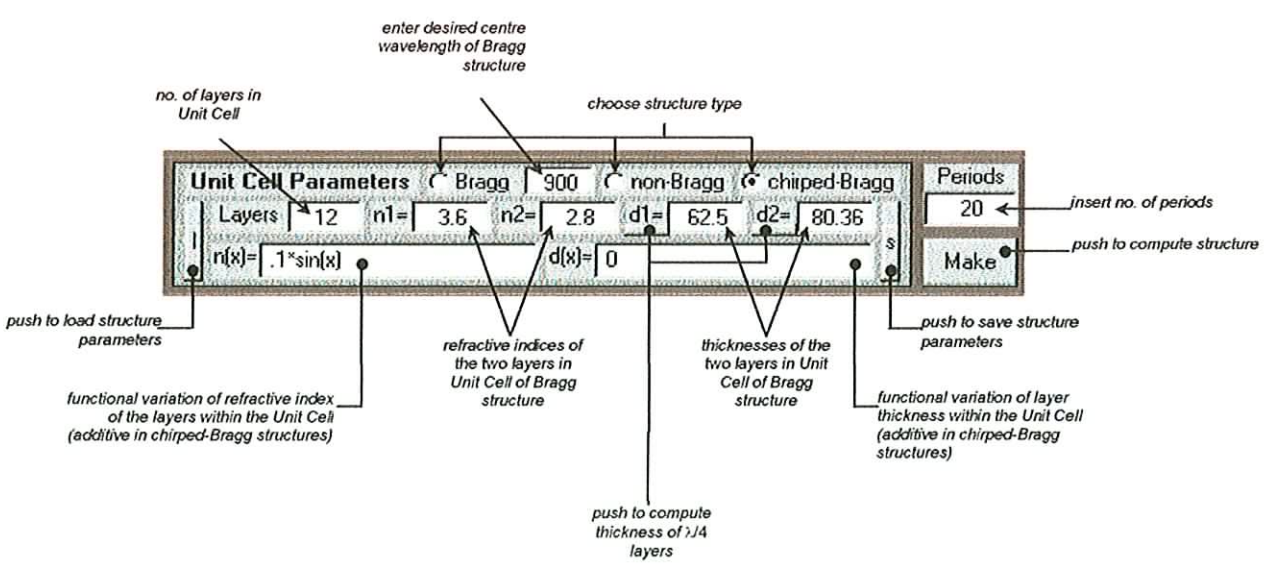

Appendix C

- Measured transmittance data, $T_{measured}$, were obtained for each material with a particular thickness.
- Reflectance is calculated from the following equation: $R = \left(\frac{n-1}{n+1}\right)^2$
- Absorbance is simply: $A = 1\text{-}R\text{-}T_{measured}$.
- The coefficient of absorption is defined as:

  $\alpha = -\frac{\ln A}{s}$, where s is the layer thickness of the material used to obtain the measured transmittance, and by plotting a graph of α versus wavelength, the best-fitted equation was obtained.
- Finally the imaginary part of the complex refractive index is: $n_I = \frac{\alpha \cdot \lambda}{4 \cdot \pi}$.

Summary:

The real parts of the complex refractive indices of Zinc Sulfide and Magnesium Fluoride [40,41] as a function of wavelength are listed below. By plotting the experimental values for both n and α against λ, the equations of the best-fitted curve of each graph using Excel are:

$$n_{(ZnS)} = 2.3229 - \frac{102.47}{\lambda} + \frac{7.56 \cdot 10^4}{\lambda^2}$$

$$n_{(MgF2)} = 1.373 + \frac{6.393}{\lambda} - \frac{882.57}{\lambda^2} + \frac{3.86 \cdot 10^5}{\lambda^3}$$

Their absorption coefficient: $\alpha_{(ZnS)} = -1.82\ 10^{-7} + 7.23\ 10^{-10}\ \lambda$ (nm^{-1})

$$\alpha_{(MgF2)} = 17.49 - 1.449 \cdot 10^{-3}\ \lambda + 7.68 \cdot 10^{-7}\ \lambda^2\ (nm^{-1})$$

Appendix D

<Program 3>

```
-------Phase angle of a 15-layered multilayer structure------

n0= 1; % refractive index of air.
ns= 1.54; % the refractive index of substrate.
a = 0; % angle of incidence
A = sqrt(8.854* 10^-12 ./(4*pi*10^-7)); % Constant
% layer's thickness vector of ZnS and MgF2 , where d(ZnS)=64
% and d(MgF2)=108 nm.
d=[64 108 64 108 64 108 64 108 64 108 64 108 64 108 64];
% refractive index vector of ZnS and MgF2, where n(ZnS)=2,34
% and n(MgF2)=1.38.
n = [2.36 1.38 2.36 1.38 2.36 1.38 2.36 1.38 2.36 1.38 2.36
     1.38 2.36 1.38 2.36];
% beginning of the "for loop" for repetitive calculations
cc=0;
for L=500:0.1:740
   M=1;
   cc=cc+1;
     for m = 1:15
        am = asin(n0*sin(a) ./n(m));
        a16 = asin(n0*sin(a) ./ns);
        k = 2*pi ./L;
        hm = n(m)*d(m)*cos(am);
        ym = A*n(m)*cos(am)
        y0 = A*n0* cos(a);
        ys = A*ns* cos(a16);
        Mm = [cos(k*hm) i*sin(k*hm)./ym; ym*i*sin(k*hm)
              cos(k*hm)];
        M = Mm*M;

     end

   % Transmitivity
   t = 2*y0 ./(y0*M(1,1) + y0*ys*M(1,2) + M(2,1) + ys*M(2,2));
   % reflectivity
   r = (y0*M(1,1) + y0*ys*M(1,2) - M(2,1) - ys*M(2,2))
        ./(y0*M(1,1) + y0*ys*M(1,2) + M(2,1) + ys*M(2,2));
    % Z is the phase angle of the transmitted light through the
   % structure.
   % X is the phase angle of the reflected light from the
   % structure
   % t and r are complex numbers.
```

```
    Z= angle(t);
    X=angle(r);
    XX(cc)=X; LL(cc)=L; ZZ(cc)= Z;
end
% the plots of the graphs are ready, but another function has
% been introduced while plotting these curves in order to
% smooth them.
% This function called "unwrap", and what it does is: to
% eliminate any sudden jump unnecessary.
figure
plot(LL,unwrap(ZZ));
title('Phase angle against wavelength');
xlabel('Wavelength(nm)');
ylabel('Phase angle [radians]');
```

<Program 4>

```
--------Phase angle of a quartz quarter-waveplate--------

%refractive indices of incident and exit media (air in this
%case)
n0=1; ns=1;
a =0; % angle of incident
A = sqrt(8.854* 10^-12 ./(4*pi*10^-7)); %constant
% no is the ordinary refractive index of quartz.
no=1.543;
% ne is the extraordinary refractive index of quartz
ne=1.553;
% d is the thickness of the quartz quarter wavelplate that
% will a phase shift of 11.pi/2.  This value was chosen only
% as an example for multiple order waveplate.
d =779.2;
% same loop "for" for repetitive calculations
% In this program, reflectivity and transmitivity are both
% calculated with the same way as in program 1 or 2 where e
% and o notations were attributed to extraordinary and
% ordinary components respectively

cc=0;
for L=580:0.1:640
   cc=cc+1;
      ae = asin(n0*sin(a)./ne);
      a2 = asin(n0*sin(a)./ns);
      he = ne*d*cos(ae);
      ye = A*ne*cos(ae);
      ye0 = A*n0* cos(a);
      yes = A*ns* cos(a2);
      k = 2*pi ./L;
      Me = [cos(k*he) i*sin(k*he)./ye; ye*i*sin(k*he)
       cos(k*he)];
      ao = asin(n0*sin(a)./no);
      ho = no*d*cos(ao);
      yo = A*no*cos(ao);
      yo0 = A*n0*cos(a);
      yos = A*ns*cos(a2);

     Mo= [cos(k*ho) i*sin(k*ho)./yo; yo*i*sin(k*ho)
     cos(k*ho)];

     te = 2*ye0 ./(ye0*Me(1,1) + ye0*yes*Me(1,2) + Me(2,1) +
     yes*Me(2,2));
```

```
        to = 2*yo0 ./(yo0*Mo(1,1) + yo0*yos*Mo(1,2) + Mo(2,1) +
        yos*Mo(2,2));

         Z=angle(te);
         X=angle(to);
         V=X-Z;
         ZZ(cc)=Z; XX(cc)=X; VV(cc)=V; LL(cc)=L;
end
% the unwrap function will be applied all the time to
% eliminate any sudden jump in the graph.
figure
plot(LL,unwrap(XX),'r',LL,unwrap(ZZ),'b');
title('Phase angle against Wavelength of the q.q.w.p only');
xlabel('Wavelength(nm)');
ylabel('Phase angle [radians]');
```

<Program 5>

------ Phase angle of a thin quartz quarter-wave plate in a multilayer cavity----------

```
% In this program the phase angle of a thin quartz-wave plate
% sandwiched between two mirrors of nine alternating layers of
% ZnS and MgF2 each.
% The calculations were done as in the previous program.

n0=1.54; ns=1.54;
a = 0;
A = sqrt(8.854* 10^-12 ./(4*pi*10^-7));
no=[2.36 1.38 2.36 1.38 2.36 1.38 2.36 1.38 2.36 1.54 2.36
    1.38 2.36 1.38 2.36 1.38 2.36 1.38 2.36];
ne=[2.36 1.38 2.36 1.38 2.36 1.38 2.36 1.38 2.36 1.55 2.36
    1.38 2.36 1.38 2.36 1.38 2.36 1.38 2.36];
d= [63.56 108.7 63.56 108.7 63.56 108.7 63.56 108.7 63.56 97.4
    63.56 108.7 63.56 108.7 63.56 108.7 63.56 108.7 63.56];
cc=0;
for L=450:0.1:800
   Me=1; Mo=1;
   cc=cc+1;
    for m = 1:19
       aem = asin(n0*sin(a) ./ne(m));
       a20 = asin(n0*sin(a) ./ns);
       hem = ne(m)*d(m)*cos(aem);
       yem = A*ne(m)*cos(aem);
       ye0 = A*n0* cos(a);
       yes = A*ns* cos(a20);
       k = 2*pi ./L;

  Mem = [cos(k*hem) i*sin(k*hem)./yem; yem*i*sin(k*hem)
        cos(k*hem)];
   Me= Mem*Me;
       aom = asin(n0*sin(a) ./no(m));
       a20 = asin(n0*sin(a) ./ns);
      hom = no(m)*d(m)*cos(aom);
       yom = A*no(m)*cos(aom);
       yo0 = A*n0* cos(a);
       yos = A*ns* cos(a20);

 Mom = [cos(k*hom) i*sin(k*hom)./yom; yom*i*sin(k*hom)
         cos(k*hom)];
  Mo= Mom*Mo;

  end
```

```
    te = 2*ye0 ./(ye0*Me(1,1) + ye0*yes*Me(1,2) + Me(2,1) +
         yes*Me(2,2));
    to = 2*yo0 ./(yo0*Mo(1,1) + yo0*yos*Mo(1,2) + Mo(2,1) +
         yos*Mo(2,2));
         Z=angle(te); X=angle(to);

         ZZ(cc)=Z; XX(cc)=X; LL(cc)=L;

end

figure

plot(LL,unwrap(ZZ),'r',LL,unwrap(XX),'b');
```

<Program 6>

```
-------Phase shift of a multilayer cavity with PVA-------

% The same presentation of calculations carried out in the
% previous program is shown in this program. Instead a PVA
% film.
% was used instead of the quartz quarter waveplate.
% The scanning region is very small in order to see the
% spectral shift of the whole structure.

n0=1.54; ns=1.54;
a = 0;
A = sqrt(8.854* 10^-12 ./(4*pi*10^-7));
no=[2.36 1.38 2.36 1.38 2.36 1.38 2.36 1.38 2.36 1.38  2.36
    1.52 2.36 1.38 2.36 1.38 2.36 1.38 2.36 1.38 2.36 1.38
    2.36];
ne=[2.36 1.38 2.36 1.38 2.36 1.38 2.36 1.38 2.36 1.38 2.36
    1.52055 2.36 1.38 2.36 1.38 2.36 1.38 2.36 1.38 2.36 1.38
    2.36];
d= [75.21 128.6 75.21 128.6 75.21 128.6 75.21 128.6 75.21
    128.6 75.21 0.29*10^6 75.21 128.6 75.21 128.6 75.21 128.6
    75.21 128.6 75.21 128.6 75.21];
cc=0;
for L=680:0.0001:682
   Me=1;
   Mo=1;
   cc=cc+1;
   for m = 1:23
      aem = asin(n0*sin(a) ./ne(m));
       a24 = asin(n0*sin(a) ./ns);

       hem = ne(m)*d(m)*cos(aem);

       yem = A*ne(m)*cos(aem);
       ye0 = A*n0* cos(a);
       yes = A*ns* cos(a24);
       k = 2*pi ./L;
       Mem = [cos(k*hem) i*sin(k*hem)./yem;  yem*i*sin(k*hem)
              cos(k*hem)];

       Me= Mem*Me;

       aom = asin(n0*sin(a) ./no(m));
       a24 = asin(n0*sin(a) ./ns);
       hom = no(m)*d(m)*cos(aom);
```

```
        yom = A*no(m)*cos(aom);
        yo0 = A*n0* cos(a);
        yos = A*ns* cos(a24);

        Mom = [cos(k*hom) i*sin(k*hom)./yom;   yom*i*sin(k*hom)
               cos(k*hom)];

        Mo= Mom*Mo;

    end
      te = 2*ye0 ./(ye0*Me(1,1) + ye0*yes*Me(1,2) + Me(2,1) +
           yes*Me(2,2));

      to = 2*yo0 ./(yo0*Mo(1,1) + yo0*yos*Mo(1,2) + Mo(2,1) +
           yos*Mo(2,2));

      Te=te*conj(te);

      To=to*conj(to);
      Z=angle(te);
      X=angle(to);
      V=X-Z;

      TTe(cc)=Te;
      TTo(cc)=To;

      ZZ(cc)=Z;
      XX(cc)=X;
      VV(cc)=V;
      LL(cc)=L;

end
figure
plot(LL,unwrap(VV));
title('Total phase shift of the whole structure');
xlabel('Wavelength(nm)');
ylabel('Total phase /rad');
```

<Program 7>

----------Birefringence and phase shift of the whole structure----------

```
% The effect of the birefringence of a material on phase shift analysis is demonstrated in this
% program.
% The material used for this study was quartz, because it has a bigger birefringence.
% The calculations were carried out as usual for all the optical parameters i.e. R and T.

n0=1.54;
ns=1.54;
a = 0;
A = sqrt(8.854* 10^-12 ./(4*pi*10^-7));
no=[2.36 1.38 2.36 1.38 2.36 1.38 2.36 1.38 2.36 1.38 2.36
    1.52 2.36 1.38 2.36 1.38 2.36 1.38 2.36 1.38 2.36 1.38
    2.36];
ne1=[2.36 1.38 2.36 1.38 2.36 1.38 2.36 1.38 2.36 1.38 2.36
    1.52055 2.36 1.38 2.36 1.38 2.36 1.38 2.36 1.38 2.36 1.38
    2.36];
ne2=[2.36 1.38 2.36 1.38 2.36 1.38 2.36 1.38 2.36 1.38 2.36
    1.525 2.36 1.38 2.36 1.38 2.36 1.38 2.36 1.38 2.36 1.38
    2.36];
ne3=[2.36 1.38 2.36 1.38 2.36 1.38 2.36 1.38 2.36 1.38 2.36
    1.55 2.36 1.38 2.36 1.38 2.36 1.38 2.36 1.38 2.36 1.38
    2.36];
d= [75.21 128.6 75.21 128.6 75.21 128.6 75.21 128.6 75.21
    128.6 75.21 0.29*10^6 75.21 128.6 75.21 128.6 75.21 128.6
    75.21 128.6 75.21 128.6 75.21];

cc=0;
for L=720:0.001:721.2
   Me1=1; Me2=1; Me3=1; Me4=1; Me5=1; Me6=1;
   Mo=1;
    cc=cc+1;
    for m = 1:23
       ae1m = asin(n0*sin(a)./ne1(m));
       a24 = asin(n0*sin(a)./ns);
       he1m = ne1(m)*d(m)*cos(ae1m);
       ye1m = A*ne1(m)*cos(ae1m);
       ye10 = A*n0* cos(a);
       ye1s = A*ns* cos(a24);
       k = 2*pi ./L;

       Me1m = [cos(k*he1m) i*sin(k*he1m)./ye1m;
              ye1m*i*sin(k*he1m) cos(k*he1m)];

       Me1= Me1m*Me1;
```

```
    ae2m = asin(n0*sin(a) ./ne2(m));
    a24 = asin(n0*sin(a) ./ns);
    he2m = ne2(m)*d(m)*cos(ae2m);
    ye2m = A*ne2(m)*cos(ae2m);
    ye20 = A*n0* cos(a);
    ye2s = A*ns* cos(a24);
    k = 2*pi ./L;

    Me2m = [cos(k*he2m) i*sin(k*he2m)./ye2m;
           ye2m*i*sin(k*he2m) cos(k*he2m)];

    Me2= Me2m*Me2;

    ae3m = asin(n0*sin(a) ./ne3(m));
    a24 = asin(n0*sin(a) ./ns);
    he3m = ne3(m)*d(m)*cos(ae3m);
    ye3m = A*ne3(m)*cos(ae3m);
    ye30 = A*n0* cos(a);
    ye3s = A*ns* cos(a24);
    k = 2*pi ./L;

    Me3m = [cos(k*he3m) i*sin(k*he3m)./ye3m;
           ye2m*i*sin(k*he3m) cos(k*he3m)];

    Me3= Me3m*Me3;

    aom = asin(n0*sin(a) ./no(m));
    a24 = asin(n0*sin(a) ./ns);
    hom = no(m)*d(m)*cos(aom);
    yom = A*no(m)*cos(aom);
    yo0 = A*n0* cos(a);
    yos = A*ns* cos(a24);
    k = 2*pi ./L;
    Mom = [cos(k*hom) i*sin(k*hom)./yom; yom*i*sin(k*hom)
           cos(k*hom)];

    Mo = Mom*Mo;

end
    te1 = 2*ye10 ./(ye10*Me1(1,1) + ye10*ye1s*Me1(1,2) +
          Me1(2,1) + ye1s*Me1(2,2));
    te2 = 2*ye20 ./(ye20*Me2(1,1) + ye20*ye2s*Me2(1,2) +
          Me2(2,1) + ye2s*Me2(2,2));
    te3 = 2*ye30 ./(ye30*Me3(1,1) + ye30*ye3s*Me3(1,2) +
          Me3(2,1) + ye3s*Me3(2,2));
```

```
        to = 2*yo0 ./(yo0*Mo(1,1) + yo0*yos*Mo(1,2) + Mo(2,1) +
             yos*Mo(2,2));

        Z1=angle(te1); Z2=angle(te2); Z3=angle(te3);
        X=angle(to);
        V1=Z1-X;
        V2=Z2-X;
        V3=Z3-X
        Te1=te1*conj(te1);
        Te2=te2*conj(te2);
        Te3=te3*conj(te3);
        To=to*conj(to);
      VV1(cc)=V1;
      VV2(cc)=V2;
      VV3(cc)=V3;

      XX(cc)=X;

      TTe1(cc)=Te1;
     TTe2(cc)=Te2;
      TTe3(cc)=Te3;
      TTo(cc)=To;
      LL(cc)=L;

end

figure
plot(LL,TTe2,'r',LL,TTe4,'b',LL,TTo,'g');
title('Phase difference between the o-and e-waves against
wavelength of the whole str.');
xlabel('Wavelength(nm)');
ylabel('Phase diference [radians]');
```

Appendix F

Fabry-Perot Interferometer

The Fabry Perot (FP) is a high-resolution optical spectrometer that works on the principle of constructive interference [20]. Given a monochromatic point source, imaged through a conjugate lens pair (with the interferometer in between), the rays either constructively or destructively interfere in the interferometer. Thus a bright or dark spot is seen at the image plane. With a distributed monochromatic source, different rays travel different path lengths inside the cavity, and the FP becomes an angle filter, resulting in the characteristic circular "Airy" fringe pattern.

The Fabry-Perot interferometer was designed first in 1899 by C. Fabry and A. Perot. Two partial mirrors are aligned parallel to one another, forming a reflective cavity. Figure 9. 1 shows an incident ray of light entering such a cavity and reflecting back and forth inside. At each reflection, part of the beam is transmitted, splitting each incident ray into a series of rays. Since the transmitted rays are all split from a single incident ray, they have a constant phase relationship (assuming a sufficiently coherent light source is used). The general theory behind interferometry still applies to the Fabry-Perot model, however, these multiple reflections reinforce the areas where constructive and destructive effects occur making the resulting fringes much more clearly defined

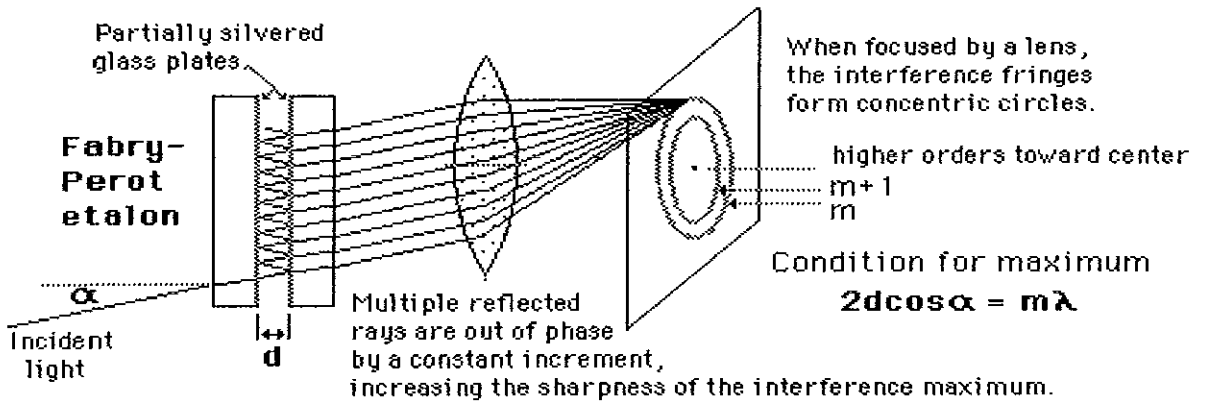

Fig. 9.1. Schematic diagram of a Fabry-Perot etalon.

Circular fringes only occur when these plates are parallel, and if the plates of the Fabry-Perot device are moveable (i.e. it is an interferometer), then the fringes will move across the surface due to the change in constructive and destructive interference lengths. A photodiode, or photoelectric device, may be placed at the centre of the interference fringes, which will count the fringes as they pass by. If the distance the plate has moved by is precisely known, then it is possible to calculate the unknown wavelength of some source by order of interference relationship $\lambda = 2L \quad n$, where:

n: the order of interference, or the number of fringes that pass by in our case.

L represents the distance travelled by the mirror.

Another unique characteristic of Fabry-Perot Interferometer is the Free Spectral Range. This also has to do with fringe frequency, and is defined as the separation between adjacent orders of interference. This definition refers to how far the moving mirror must move to arrive at the next order of constructive interference which occur every $n\lambda \quad 2$. This relationship says that orders of constructive interference occur every half-multiple of the wavelength of the studied light.

Finally, the resolving power of the Fabry-Perot device may be defined as the ability to differentiate between adjacent fringe systems. Imagine for an instant, that a photodetector device is placed so that it is detecting the fringes that go by while one of the reflective, planar surfaces is being moved.

This change in fringe maxima can be modelled mathematically by what is known as an Airy function in the form $(1+Fsin^2 \Delta / 2)^{-1}$. The delta term represents the length for a change in order of constructive interference and occurs in integer multiples of π. The reason why half of this distance is chosen is because that satisfies the Taylor criterion for the definition of resolution. According to these standards, two lines are considered to be resolved if the individual curves of the Airy function cross at the half intensity point (occurs at half the length of order of constructive interference). Thus, if attempting to resolve two sets of fringes, the total intensity observed will be represented as the sum of two Airy Functions as follows:

$$I_t = I_0(1 + FSin^2 \frac{\Delta}{2})^{-1} + I_0(1 + FSin^2 \frac{\Delta'}{2})^{-1}$$

Here, F is termed the coefficient of finesse and is equal to $F = 4R/(1-R)^2$, where the term R represents the reflectance of the planar surfaces in the Fabry-Perot device. When F is small, the fringes will appear smeared and indistinguishable, and when F is larger peaks get sharper and distinguishable 2π.

Appendix G

Distributed Bragg Reflector (DBR)

A simple DBR consists of multiple layers of alternating high-and low-index materials arranged periodically. The thickness of each layer is chosen so as to satisfy the Bragg quarter-wave condition: $d = \frac{\lambda_0}{4n}$

where λ_0 is the reference wavelength of the structure, and d and n are the thickness and the real part of the linear refractive index of a particular layer, respectively.

By growing two regular Distributed Bragg Reflector (DBR) mirrors, and put them together as a sandwich with a space between we will be able to create a Fabry-Perot Microcavity (FPM) structure.

A schematic diagram of a typical grown mirror used in this project, which is a stack of alternate high- and low-index films, all one-quarter-wavelength thick is shown below.

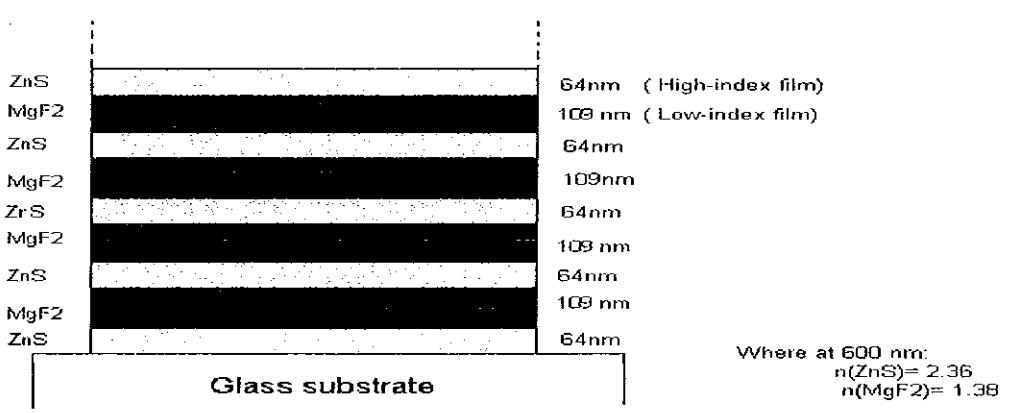

Fig.7.4. A stack of alternate high and low index films, all one-quarter wavelength thick.

Where the reference wavelength of the structure was chosen to be $\lambda_0 = 600$ nm for simplicity, and at $\lambda_0 = 600$ nm, the refractive indices of the materials to be evaporated (Zinc Sulphide, ZnS, and Magnesium Fluoride, MgF_2) are 2.36 and 1.38 respectively. Therefore the desired layer thicknesses ($d = \frac{\lambda_0}{4n}$) are 64 and 109 nm for ZnS and MgF_2 respectively.

To investigate the propagation of light in multilayer structure and to show how the phase shift varies at successive boundaries throughout the assembly, consider the following diagram, figure 2.

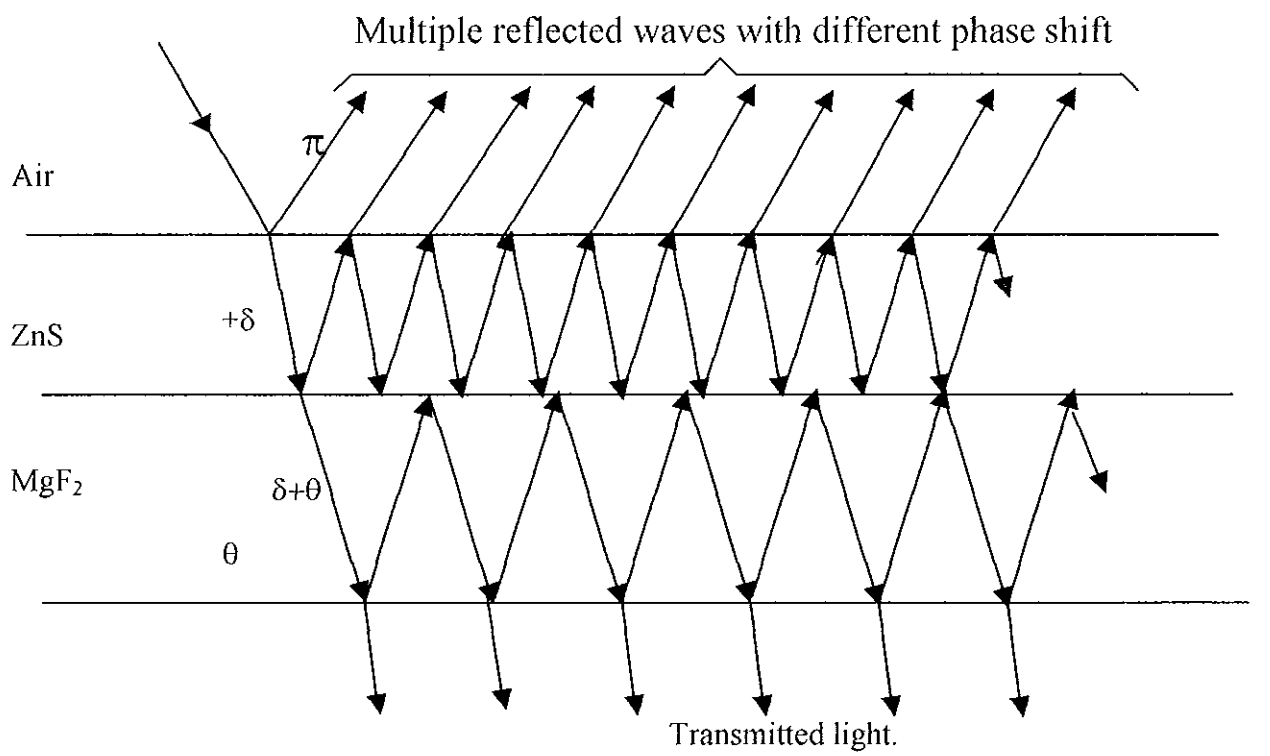

Fig.7.5. Variable changes in phase shift associated with multiple reflections make theoretical calculations more complicated, where +δ is the initial phase of the incident light and θ is the phase shift of the beam coming with a phase of +δ.

When light strikes the first surface of the structure some of it is reflected with a phase shift of π and the rest is refracted and passes through the ZnS layer with the initial phase of the incident light $+\delta$, because there is no phase change on transmission. The beam itself with a phase of $+\delta$ will undergo reflection and refraction at the second boundary with a different phase shift and so on. These multiple reflections from each boundary will reappear at the front surface all in phase so that they will recombine constructively.

As by definition, the phase angle of a complex number $Z = a + ib$ is simply:

$$\varphi = \tan^{-1}(b/a)$$

These will apply to the computed transmission and reflectance vectors to find out the phase angle on transmission and on reflection.